Modeling Fixed-Bed Coal Gasifiers

Michael L. Hobbs, Predrag T. Radulovic, and L. Douglas Smoot
Advanced Combustion Engineering Research Center, Brigham Young University, Provo, UT 84602

A one-dimensional model of countercurrent fixed-bed coal gasification has been developed, and results have been compared to experimental data from commercial-scale gasifiers. The steady-state model considers separate gas and solid temperatures, axially variable solid and gas flow rates, variable bed void fraction, coal drying, devolatilization based on chemical functional group composition, oxidation and gasification of char, and partial equilibrium in the gas phase. Generalized treatment of gas-phase chemistry and accounting for variable bed void fraction were necessary to predict realistic axial temperature and pressure profiles in an atmospheric fixed-bed gasifier. Model evaluation includes sensitivity of axial temperature profiles to model options, model parameters and operational parameters. Model predictions agree reasonably well with experimental temperature and pressure profile data for gasification of eight coal types ranging from lignite to bituminous. The relative importance of char oxidation resistances to bulk film diffusion, ash diffusion, and chemical reaction is identified.

Introduction

Fixed-bed systems are simple and reliable, have high thermal efficiency, and require minimal pretreatment of feed coal. Combustion and gasification of coal in fixed or slowly moving beds of packed coal particles are of substantial commercial interest. Such beds can be operated at high pressure, providing opportunity for increased power generation efficiency through combined cycle processes. Fixed beds are also a popular choice for mild gasification since, by their countercurrent nature, the liquids can be quickly removed before being altered by substantial reaction. The U.S. Clean Coal Technology demonstration program includes two fixed-bed gasifier processes undergoing commercial demonstration.

In a large-scale, fixed-bed gasifier, Figure 1, coal is fed to the top of the reactor and moves downward under gravity, countercurrent to the rising gas stream. The dry or slagging ash is removed at the bottom of the reactor. The feed gas is commonly composed of air or oxygen and steam. Excess steam is supplied to the gasifier to control the ash temperature. Figure 1 also shows the reactor divided into four overlapping zones: drying, devolatilization, gasification, and combustion. As the coal slowly descends, the hot gases produced in the gasification and combustion zones exchange energy with the colder solid. Water and subsequently volatile matter are released when the solid reaches sufficiently high temperatures. After drying and devolatilization, the char enters the gasification zone where carbon reacts with steam, carbon dioxide, and hydrogen. Endothermic reactions in this section produce carbon monoxide

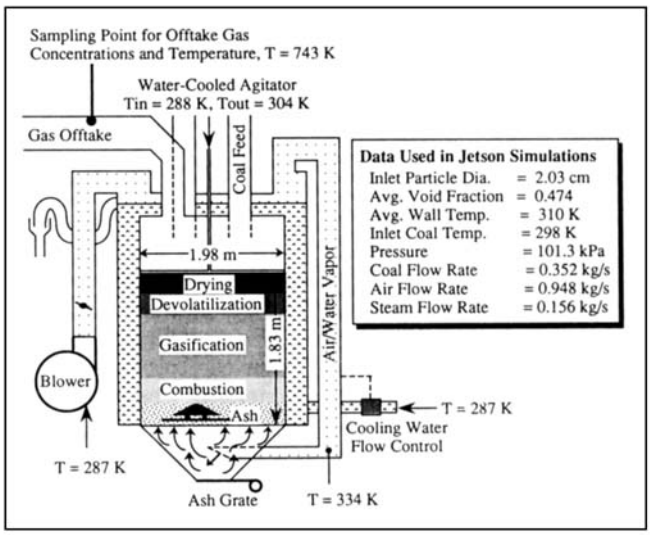

Figure 1. Typical atmospheric fixed-bed gasifier (Wellman-Galusha).

Temperatures are for gasification of Jetson coal blown with air. Configuration and data taken from Thimsen et al. (1984).

Correspondence concerning this article should be addressed to L. D. Smoot.
M. L. Hobbs is presently at the Sandia National Laboratories, P. O. Box 5800, Div. 1512, Albuquerque, NM 87185.

and hydrogen. The slightly exothermic reaction of hydrogen with carbon produces methane. Differentiation between the "gasification zone" and "combustion zone" is based on the presence or absence of free oxygen. Combustion and gasification reactions occur simultaneously in the "combustion zone." Combustible gases such as carbon monoxide or hydrogen may react with oxygen. The exothermic combustion reactions provide the necessary energy for the endothermic gasification reactions and drying. Blast gas, which is composed of steam and oxidant (air or oxygen), is preheated by the hot ash. Part of the process steam is produced by a water jacket surrounding the gasification chamber.

Solid residence times in the drying, gasification and oxidation zones may be on the order of several hours. Residence time in the ash layer may be even higher depending on the thickness of this zone. Large solid residence times indicate significant settling resulting in variable axial velocities. Gas residence times are on the order of seconds. Both solid and gas heating rates are most dramatic in the devolatilization and the oxidation zones. Typical solid heating rates are smaller than 10 K/s, while gas heating rates are up to 10,000 K/s.

Existing fixed-bed models in the open literature show that all fixed-bed models were qualitative until the late 1970s. At that time, Winslow (1976) presented a detailed model for underground coal gasification. Soon afterward, Amundson and Arri (1978), Yoon et al. (1978), Desai and Wen (1978), and Stillman (1979) presented detailed models of a fixed-bed gasifier. Cho and Joseph (1981) extended Yoon's model to include unequal gas-solid temperatures. Yoon's model was further extended by Kim and Joseph (1983) to account for transient effects. Yu et al. (1983) extended Yoon's model to two space dimensions. More recent models include the one-dimensional, steady-state model of Earl and Islam (1985) and the two-dimensional, transient models of Thorsness and Kang (1986) and Bhattacharya et al. (1986). Khanna and Seinfeld (1987) discussed recent advances in catalytic fixed-bed reactor models which have many of the features of coal gasification/combustion fixed-bed models discussed earlier. Smoot and Smith (1985), Hobbs (1990), and Radulovic et al. (1992) have reviewed fixed-bed modeling.

Previous fixed-bed models share common assumptions such as equal gas/solid temperatures, axially uniform gas/solid-phase plug flow, uniform bed porosity, instantaneous devolatilization (with percent volatiles from proximate analysis), combustion/gasification by shell progressive or ash segregation submodels, kinetic parameters from small particle data, and little or no gas-phase chemistry. The fixed-bed model discussed here eliminates most of these assumptions. The primary contribution of this article is the development and evaluation of an improved, comprehensive fixed-bed model that utilizes an advanced, coal-general devolatilization submodel.

One-Dimensional Fixed-Bed Model

Conservation equations

The conservation equations for mass and energy form the foundation of the model. The derivation of the two-phase conservation equations can be found in Crowe and Smoot (1979). The source terms in the continuity and energy equations are described by physical and chemical submodels. Input parameters are reactor dimensions, operating conditions, inlet solid and gas temperatures, pressure, concentrations, flow rates, and wall temperature. Calculated quantities include axial variation in gas temperature, solids temperature, pressure, species concentration, gas-flow rate, solid flow rate, and wall heat loss. Plug flow is assumed in both the solid and gas phases with variable axial velocities. Gas-phase pressure drop is calculated with the Ergun equation for packed beds (Ergun, 1952). An effective heat-transfer coefficient is used for heat loss to the wall, including both stagnant and dynamic contributions for convective and radiative transfer. Large coal particle devolatilization is allowed to occur simultaneously with char oxidation and gasification. Shell progressive or ash segregation, shrinking core char submodels describe oxidation and gasification. Chemical equilibrium is used to calculate gas concentrations and temperatures. Turbulence is not treated formally in the slowly moving bed with low gas velocities, but is included implicitly through model correlations such as the effective heat-transfer coefficient. Primary assumptions for the one-dimensional fixed-bed model include negligible aerodynamic drag, ideal gases, and particles locally isothermal throughout; one particle size and type exist in the feed coal. This model will be referred to as MBED-1D (moving-bed, one-dimensional) here. The reactor, however, is frequently referred to as a fixed-bed reactor because of the large difference in gas- and solid-phase residence times. Assumptions are discussed in detail by Hobbs (1990).

The conservation equations and boundary conditions for the one-dimensional, fixed-bed model are given in Table 1. These can be classified as gas and solid overall continuity, gas and solid energy equations, and gas and solid species or elemental continuity equations. The constitutive relations for solid flow have been proposed only recently, and no solution for these equations has been attempted (Gray and Stiles, 1988). Thus, only differential equations for continuity and energy are treated in the model described here.

The overall gas and solid species continuity equations are given in Eqs. 1 and 2 in Table 1. The gas and solid flow rates are represented by W_g (kg/s) and W_s (kg/s), respectively. The axial distance and cross-sectional areas are represented by z (m) and A (m^2), respectively. The volumetric reaction rate is represented by r_i ($kg/m^3 \cdot s$) where i depicts the different heterogeneous reactions such as drying, char oxidation, char gasification, and devolatilization. Reaction rates are written as the rate of mass addition to the gas phase per unit volume per unit time; thus, a positive rate indicates a source of mass for the gas phase and a sink for the particle phase.

The gas and solid energy equations are given by Eqs. 3 and 4 in Table 1. The total gas and solid enthalpies are represented by h_g (J/kg) and h_s (J/kg). The energy exchange between solid and gas is represented by Q_{sg} (W/m^3). Heat losses to the walls from the gas and solid phases are represented by Q_{gw} (W/m^3) and Q_{sw} (W/m^3), respectively. Calculation of Q_{sg}, Q_{gw}, and Q_{sw} will be discussed subsequently. The last term in the energy equation represents the energy exchange due to chemical reaction and accounts for mass loss from the particle phase and mass addition to the gas phase. This reaction term can be calculated by performing an energy balance around the particle/gas interface as discussed in detail by Hobbs (1990). The gaseous reactants are assumed to be at the gas temperature, and the reaction is assumed to take place at the solid temperature. A sample calculation associated with the term $r_i h_{ig}$ for the oxidation reaction is given by Hobbs (1990).

Table 1. Differential Equation Set and Boundary Conditions for MBED-1D

Overall Gas Species Continuity	$\frac{dW_g}{dz} = A\sum_{i=1}^{n} r_i$	(1)
Overall Solid Species Continuity	$\frac{dW_s}{dz} = -A\sum_{i=1}^{n} r_i$	(2)
Gas-Phase Energy	$\frac{dW_g h_g}{dz} = A\left(Q_{sg} - Q_{gw} + \sum_{i=1}^{n} r_i h_{ig}\right)$	(3)
Solid-Phase Energy	$\frac{dW_s h_s}{dz} = A\left(-Q_{sg} - Q_{sw} + \sum_{i=1}^{n} r_i h_{ig}\right)$	(4)
Solid Species Continuity		
Moisture	$\frac{dW_{\text{moisture}}}{dz} = -Ar_{\text{moisture}}$	(5)
Nonvolatile carbon	$\frac{dW_{\text{Nonvolatile C}}}{dz} = -Ar_{\text{Nonvolatile C}}$	(6)
Nonvolatile sulfur	$\frac{dW_{\text{Nonvolatile S}}}{dz} = -Ar_{\text{Nonvolatile S}}$	(7)
Organic functional groups	$dy_i/dz = -(1/u_s)k_i y_i$	(8-26)
Tar fraction	$dx/dz = -(1/u_s)k_x x$	(27)
Gas-Phase Elemental Continuity*	$\frac{dW_g \omega_j}{dz} = A\sum_{i=1}^{n} r_{i,j}$	(28-32)
Gas-Phase Tar Species Continuity	$\frac{dW_{\text{tar}}}{dz} = A\sum_{i=1}^{n} r_{i,\text{tar}}$	(33)
Gas-Phase Tar Elemental Continuity*	$\frac{dW_{\text{tar}}\omega_{\text{tar},j}}{dz} = A\sum_{i=1}^{n} r_{i,j}^{\text{tar}}$	(34-38)
Boundary Conditions		
Overall solid/gas species continuity	Feed coal/gas weight flow rate	
Solid/gas-phase energy	Feed coal/gas enthalpy or temperature	
Solid species continuity	Proximate and functional group analysis	
Gas-phase elemental and tar continuity	Feed gas and tar composition	

*j represents carbon, hydrogen, nitrogen, oxygen, and sulfur.

Auxiliary equations

Pressure Drop. The pressure drop in the reactor is calculated from Ergun's equation (Ergun, 1952) since Reynolds numbers are typically less than 500 in fixed-bed coal gasifiers. The small pressure drop in the reactor is sensitive to the bed void fraction, ϵ. Void fractions of the feed coal at the bed top and the product ash at the bed bottom were estimated based on coal and ash bulk and apparent density measurements. The void fraction was assumed to vary linearly from the top to the bottom of the bed. In two sets of independent measurements, Krishnudu et al. (1989) stopped coal bed reaction and measured bed void fraction along the bed length, which was shown to vary linearly from the top to the bottom of the bed. Subsequent comparisons with pressure drop measurements provide support for this approach.

Gas-Phase Chemistry. Gas temperature is determined by assuming all gas species to be in thermal equilibrium and partial or total chemical equilibrium. Gas-phase composition is determined by Gibbs free energy minimization. Solid temperature is determined from the solid enthalpy and the elemental composition of the coal. All gas-phase transport properties (such as conductivity, viscosity, and diffusivity) are considered to be functions of both temperature and composition. Partial equilibrium refers to a gaseous mixture where at least one species is held out of chemical equilibrium. Hobbs et al. (1992) investigated three options regarding equilibrium: total equilibrium, partial equilibrium where tar was held out of chemical equilibrium, and partial equilibrium where all gases in the drying and devolatilization zone were assumed to be nonreactive. Since gas-phase kinetic models for coal systems are complex, the one-dimensional fixed-bed model assumes partial equilibrium by holding tar out of chemical equilibrium.

Mass and Heat Transfer. Mass- and heat-transfer processes in fixed-bed gasifiers are affected by complex solids flow and chemical reactions. Coarsely crushed coal settles while undergoing heating, drying, devolatilization, gasification, and combustion. Coal particles change in diameter, shape, and porosity. Nonideal behavior may result from coal bridges, gas bubbles, and channels. Variable bed void fraction may also change heat- and mass-transport properties. Correlations for solid-to-gas heat-transfer coefficients are questionable, since they are typically obtained under ideal conditions. Mass transfer occurs by diffusion and convection. Heat transfer is by conduction, convection, and radiation in the gas and solid phases.

Several physical properties of the gas and particle phases are required to obtain mass- and heat-transfer coefficients needed to solve the differential equation set in Table 1. Chapman-Enskog theory has been used to calculate multicomponent gas mixture viscosity and diffusivity (Bird et al., 1960). Conventional gas species and mixture conductivity, viscosity, and diffusivity methods used here are documented by Hobbs (1990). The particle is assumed to swell linearly with the extent of devolatilization. Euken's formula is used to calculate the conductivity of individual gaseous species (Bird et al., 1960). Furthermore, the gaseous tar diffusivity is assumed to be 0.1 cm^2/s at standard temperature and pressure (Suuberg et al., 1979). The pressure and temperature dependences for the tar diffusivity are assumed to follow Chapman-Enskog theory. The JANAF tables were used to provide values for calculating gas-phase enthalpy, entropy and heat capacity (Stull and

Prophet, 1971). Dulong's formula (Perry and Chilton, 1973) was used for heating value of the char, Merrick's correlations (1983) were used for char enthalpy and heat capacity, and the Kopp-Neumann rule was used for ash heat capacity (Mills and Rhine, 1989).

The heat- and mass-transfer correlations used in the one-dimensional model are summarized in Table 2. Effective axial and radial conductivities are correlated by Yagi et al. (1960), Bischoff (1962), and Froment and Bischoff (1979), respectively. Both the axial and radial effective conductivities take into account molecular as well as turbulent contributions. The effective radial conductivities of the gas and solid phases, which account for radiation, are correlated by DeWasch and Froment (1971). The mass-transfer coefficient in Table 2 is used to calculate the film resistance and the effective particle resistance to mass transport.

The effective bed-to-wall heat-transfer coefficient as well as the gas- and solid-phase contributions are determined by the correlations suggested by DeWasch and Froment (1971). The heat transfer to the wall is treated by Yagi and Wakao (1959), Yagi and Kunii (1960), and Rohsenow et al. (1985). There are no direct experimental data available on the gas- and solid-phase contributions to the bed-to-wall heat transfer. The volumetric heat-transfer rate from solid to gas, Q_{sg} (J/m^3·s), can be written as:

$$Q_{sg} = \zeta h_{sg} \pi d_p^2 \eta_p (T_s - T_g) \tag{1}$$

where ζ, h_{sg} (J/s·m^2·K), and η_p (1/m^3) represent deviations from nonreactive solid-to-gas heat transfer (ranges from 0.02 to 1.0), the nonreactive solid-to-gas heat-transfer coefficient (in Table 2), and the particle number density, respectively. The volumetric wall heat losses from the solid and gas phase, Q_{gw} and Q_{sw} (J/m^3·s), can be calculated as follows:

$$Q_{gw} = \frac{4h_w^g}{D}(T_g - T_{\text{wall}}) \tag{2}$$

Table 2. Heat- and Mass-Transport Correlations Used in MBED-1D

Bed-to-wall heat-transfer coefficient	$h_w = 2.44k_r^0 D^{-4/3} + 0.033k_g \text{PrRed}_p^{-1}$	(1)	Froment and Bischoff (1979)
Gas-to-wall heat-transfer coefficient	$h_w^g = h_w k_{rg}/(k_{rg} + k_{rs})$	(2)	DeWasch and Froment (1971)
Solid-to-wall heat-transfer coefficient	$h_w^s = h_w k_{rs}/(k_{rg} + k_{rs})$	(3)	DeWasch and Froment (1971)
Static effective radial conductivity	$k_r^0 = k_g\epsilon\left(1 + \frac{d_p h_{rv}}{k_g}\right) + \frac{k_g(1-\epsilon)}{\left(\frac{1}{\phi} + \frac{h_{rs}d_p}{k_g}\right)^{-1} + \frac{2}{3\kappa}}$	(4)	Froment and Bischoff (1979)
Gas effective radial conductivity	$k_{rg} = k_g\left\{\epsilon\left(1 + \frac{d_p h_{rv}}{k_g}\right) + 0.14\text{PrRe}/\left[1 + 46\left(\frac{d_p}{D}\right)^2\right]\right\}$	(5)	Froment and Bischoff (1979)
Solid effective radial conductivity	$k_{rs} = k_g(1-\epsilon)/\left[\left(\frac{1}{\phi} + \frac{h_{rs}d_p}{k_s}\right)^{-1} + \frac{2}{3\kappa}\right]$	(6)	Froment and Bischoff (1979)
Solid conductivity	$k_s = (\rho_s^t/4{,}511)^{3.5}\sqrt{T_s}$	(7)	Merrick (1983)
Void-to-void radiation coefficient	$h_{rv} = 2.27\times10^{-7}T_g^3/\left[1 + \frac{\epsilon}{2(1-\epsilon)}\left(\frac{1-\epsilon'}{\epsilon'}\right)\right]$	(8)	Froment and Bischoff (1979)
Solid radiation coefficient	$h_{rs} = 2.27\times10^{-7}\left(\frac{\epsilon'}{2-\epsilon}\right)T_s^3$	(9)	Froment and Bischoff (1979)
Packing parameter	$\phi = \begin{cases} \phi_2 + (\phi_1 - \phi_2)\frac{\epsilon - 0.260}{0.476 - 0.260} & \text{if } \epsilon_1 \ge \epsilon \ge \epsilon_2 \\ \phi_1 & \text{if } \epsilon > \epsilon_1 = 0.476 \\ \phi_2 & \text{if } \epsilon < \epsilon_2 = 0.260 \end{cases}$	(10)	Kunii and Smith (1960)
Loose packing parameter (for ϵ_1)	$\phi_1 = \frac{0.3525\left(\frac{\kappa-1}{\kappa}\right)^2}{1n[\kappa - 0.5431(\kappa-1)] - \frac{0.4569(\kappa-1)}{\kappa}} - \frac{2}{3\kappa}$	(11)	Kunii and Smith (1960)
Dense packing parameter (for ϵ_2)	$\phi_2 = \frac{0.07217\left(\frac{\kappa-1}{\kappa}\right)^2}{1n[\kappa - 0.9250(\kappa-1)] - \frac{0.07498(\kappa-1)}{\kappa}} - \frac{2}{3\kappa}$	(12)	Kunii and Smith (1960)
Solid-to-gas heat-transfer coefficient	$h_{sg} = \frac{2.06Cp_gG}{\epsilon}\text{Re}^{-0.575}\text{Pr}^{-2/3}$	(13)	Gupta and Thodos (1963)
Mass-transfer coefficient	$k_m = \frac{2.06G}{\epsilon\rho_g}\text{Re}^{-0.575}\text{Sc}^{-2/3}$	(14)	Gupta and Thodos (1963)
Reynolds, Prandtl and Schmidt numbers	$\text{Re} = d_pG/\mu_g$, $Pr = Cp_g\mu_g/k_g$, $\text{Sc}_i = \mu_g/\rho_g D_{im}$	(15-17)	Definitions
Conductivity ratio	$\kappa = k_s/k_g$	(18)	Definitions
Bed void fraction	ϵ = void volume/bed volume	(19)	Definitions
Coal emissivity	$\epsilon' = 0.85$	(20)	Perry and Chilton (1973)

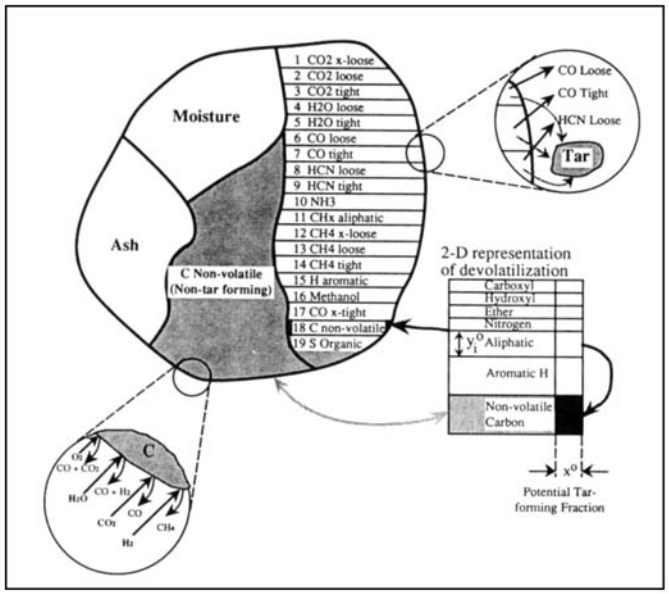

Figure 2. Coal particle with devolatilization model based on chemical functional groups (Solomon et al., 1988).

The potential tar-forming fraction of the nonvolatile carbon functional group evolves as tar. The nontar-forming C and S organic groups evolve via heterogeneous char oxidation or gasification.

$$Q_{sw} = \frac{4h_w^s}{D}(T_s - T_{\text{wall}}) \tag{3}$$

The wall temperature can be varied from the bottom of the reactor to the top of the reactor.

Coal Drying and Devolatilization. Coal reaction source terms represent drying, devolatilization, char oxidation, and gasification. These chemical and physical processes in Figure 2 show a conceptual coal particle divided into various functional groups, including moisture and ash, which is taken to be inert. Drying is assumed to be diffusion-limited (Smoot and Smith, 1979):

$$r_w = k_{wm}(\rho_{wp} - \rho_{wg}) \tag{4}$$

Blowing effects have been neglected.

As shown in Figure 2, devolatilization is described by assuming that the organic portion of the coal particle is composed of various functional groups, such as carboxyl, hydroxyl, ether, and nitrogen. A functional group model (FG model) has been used to describe the devolatilization process (Serio et al., 1987; Solomon et al., 1988). The kinetics for functional group evolution are considered to be independent of the type of coal used.

Application of the functional group devolatilization model of Solomon et al. (1988), used here, is discussed in detail by Hobbs (1990). This section describes the devolatilization rate equations which appear as source terms in the continuity equations in Table 1. The change in functional group composition and tar fraction is obtained by Eqs. 8 through 27 in Table 1. The evolution of each functional group into the gas phase is represented by first-order decay. The equations representing this first-order decay are not truly solid species conservation equations; however, Eqs. 8 through 27 are used to keep track of the functional groups in the solid phase throughout the reactor. The values for Arrhenius rate coefficients, k_i and k_x, and the initial functional group compositions, y_i^o, can be found in Hobbs (1990) or Hobbs et al. (1992).

The mass rate of change of each reactive element in the gas phase is depicted by Eqs. 28 through 32 in Table 1. Gases such as argon are inert to reaction, and a differential equation is not required to track such gases. The sources for gas-phase elements are the heterogeneous oxidation, gasification and devolatilization reactions. The only gas-phase species that is tracked throughout the reactor is tar. Tar was either assumed to be nonreactive or to react to equilibrium in the gas phase.

Predicting accurate coal volatiles yield and composition is important since as much as 40–60% of the dry, ash-free mass can be lost by devolatilization. The coal particle in Figure 2 is divided into various chemical functional groups. The X and Y values represent the two-dimensional description of coal. The Y dimension is divided into fractions according to the chemical composition of the coal. The initial fraction of a particular functional group component is represented by y_i^o, and the sum of y_i^os equals 1. The evolution of each functional group into the gas is represented by the first-order decay of the Y dimension, $dy_i/dt = -k_i y_i$. The X dimension represents nontar-forming char, tar-forming char, and tar. The evolution of tar is represented by the first-order decay of the X dimension, $dx/dt = -k_x y_i$. The potential tar-forming fraction, x^o, was calculated with the semi-empirical correlation of Ko et al. (1988) as discussed by Hobbs et al. (1992). Values for y_i^o can be found subsequently in Table 3. Normally distributed Arrhenius rate coefficients for 19 functional groups, k_i, and tar, k_x, were obtained from Solomon et al. (1988) for the organic functional groups in Figure 2.

The volumetric devolatilization rate expressions, r_i^d(kg/m^3·s) are derived by Hobbs (1990):

$$r_i^d = \rho_{sm}^o(1-\epsilon^0)(1-\Omega_{\text{ash}}^o-\Omega_{\text{moisture}}^o)[(1-x^o+x)(k_i y_i)+y_i(k_x x)] \tag{5}$$

r_i^d includes mass losses due to both light gas evolution and tar evolution, which are required by the continuity equations in Table 1. However, the tar continuity equations require the tar volumetric rate equations, $r_{i,\text{tar}}^d$ (kg/m^3·s), which are also found in Hobbs (1990):

$$r_{i,\text{tar}}^d = \rho_{sm}^o(1-\epsilon^o)(1-\Omega_{\text{ash}}^o-\Omega_{\text{moisture}}^o)k_x x y_i \tag{6}$$

Equations 5 and 6 do not explicitly include resistance due to mass transport. Saxena (1990) concludes that heat- and mass-transport limitations in large coal particles are significant. Coupling between mass transport of oxidation and gasification products and devolatilization complicates the mathematical description of both devolatilization and char oxidation. Simulations with the purely kinetic devolatilization equations as formulated above can result in unrealistically fast product evolution for large coal particles. To introduce mass transport effects, transport resistance through the film and particle is added to the Arrhenius rate expression as diffusional resistances:

Table 3. Functional Group Compositions, Calculated Potential Tar-Forming Fractions, and Ultimate Analysis*

Reactor** Functional Groups (Dry, Ash-Free)	Lurgi Rose y_i^0	WG Absal y_i^0	WG Benton y_i^0	WG Elk y_i^0	WG Jetson y_i^0	WG Kemer y_i^0	WG Leucite y_i^0	WG Rose y_i^0	WG Utah y_i^0
CO_2 extra loose	0.035	0.028	0.065	0.000	0.000	0.028	0.028	0.035	0.003
CO_2 loose	0.035	0.020	0.030	0.006	0.006	0.020	0.020	0.035	0.007
CO_2 tight	0.030	0.021	0.005	0.005	0.005	0.021	0.021	0.030	0.017
H_2O loose	0.000	0.030	0.000	0.011	0.011	0.027	0.024	0.000	0.025
H_2O tight	0.051	0.022	0.027	0.011	0.011	0.022	0.022	0.040	0.020
CO ether loose	0.055	0.050	0.060	0.050	0.050	0.050	0.050	0.055	0.025
CO ether tight	0.000	0.043	0.000	0.044	0.059	0.000	0.000	0.000	0.036
HCN loose	0.010	0.000	0.005	0.022	0.025	0.003	0.016	0.005	0.000
HCN tight	0.015	0.013	0.013	0.009	0.009	0.018	0.018	0.015	0.022
NH_3	0.001	0.001	0.001	0.000	0.000	0.001	0.001	0.001	0.000
CH_x aliphatic	0.182	0.169	0.212	0.185	0.161	0.201	0.195	0.202	0.189
CH_4 extra loose	0.000	0.000	0.000	0.020	0.020	0.000	0.000	0.000	0.000
CH_4 loose	0.022	0.017	0.017	0.015	0.015	0.017	0.017	0.022	0.022
CH_4 tight	0.012	0.008	0.009	0.015	0.015	0.008	0.008	0.012	0.022
H aromatic	0.013	0.013	0.017	0.012	0.012	0.013	0.013	0.013	0.017
CH_3OH	0.000	0.000	0.000	0.000	0.000	0.000	0.000	0.000	0.000
CO extra tight	0.000	0.043	0.090	0.020	0.020	0.043	0.043	0.000	0.040
C nonvolatile	0.522	0.518	0.440	0.565	0.565	0.518	0.518	0.522	0.548
S organic	0.017	0.004	0.009	0.009	0.016	0.010	0.006	0.013	0.006
Total	1.000	1.000	1.000	0.999	1.000	1.000	1.000	1.000	0.999
calculated x^{o*}	0.110	0.137	0.227	0.270	0.222	0.219	0.167	0.150	0.270
Coal type	Subbit	Subbit	Lig	Bit	Bit	Subbit	Subbit	Subbit	Bit
DAF ultimate									
C	0.771	0.763	0.737	0.825	0.814	0.775	0.781	0.787	0.803
H	0.049	0.051	0.062	0.057	0.051	0.056	0.050	0.049	0.062
N	0.014	0.008	0.010	0.016	0.018	0.012	0.019	0.011	0.012
O	0.150	0.174	0.182	0.093	0.102	0.147	0.144	0.140	0.117
S (organic)	0.017	0.004	0.009	0.009	0.016	0.010	0.006	0.013	0.006

*Functional group compositions were determined to match reported ultimate analysis using the criterion presented in Hobbs (1990). The semi-empirical correlation of Ko et al. (1988) was used to calculate x^o at pressures in Table 7.
**WG represents the atmospheric Wellman-Galusha Gasifier.

$$k_{i,x}^{\text{effective}} = \left(\frac{1}{k_{i,x}} + \frac{1}{k_m} + \frac{1}{k_{\text{eff}}}\right)^{-1} \tag{7}$$

where $k_{i,x}^{\text{effective}}$, $k_{i,x}$, k_m, and k_{eff} represent the effective devolatilization rate constant, the distributed Arrhenius devolatilization rate constant, the film mass-transport coefficient, and the effective internal mass-transport coefficient for the particle. The resistance through the particle is a function of the particle burnout and is negligible at the beginning of devolatilization. The mass-transfer resistances used here for devolatilization are identical to those used in the oxidation and gasification submodel and will be discussed in more detail in the following section.

Diffusional mass transport may not be an appropriate mode of transport for devolatilization. Jets of volatile gases suggest that convection may dominate mass transport for small-particle devolatilization. However, diffusion may be important for devolatilization of large particles at typical heating rates found in fixed-bed reactors. Internal particle temperature gradients may be significant during devolatilization (Phuoc and Mathur, 1991), but experimental evidence using thermocouples embedded into large coal particles during devolatilization indicates that thermal equilibrium is reached rapidly (for example, Nuttall et al., 1979).

Tar. Estimates of the tar production rate from a fixed-bed gasifier using the functional group devolatilization model have not been reliable (Hobbs, 1990). More recently, Solomon et al. (1988) and Fletcher et al. (1992) have developed network models of organic coal structure that lead to promising methods for estimating tar production rates. This new work, however, had not advanced to the point where it could be considered here. Ko et al. (1988) have published a correlation of a large quantity of tar production data, mostly on small coal particles. In our fixed-bed model, tar is either estimated from Ko et al. or provided from experimental data. In a separate study, we (Hobbs, et al., 1992) show that tar production estimated from Ko et al. was consistently higher than measured data for several coals in the Wellman-Galusha gasifier.

Oxidation and Gasification. Oxidation and gasification reactions consume the char that is assumed to be composed of nonvolatile functional groups. As shown in Figure 2, three gasification agents are considered: steam, carbon dioxide, and hydrogen. Light gases and tar competitively evolve, resulting in char. Both tar and char are treated as single species that have variable compositions depending on the location in the reactor.

The two most common char oxidation submodels used in fixed-bed coal gasification modeling are the Shell Progressive model (SP model) and the Ash Segregation model (AS model). The differences between the two models are in the description of the ash. The ash in the SP model remains intact. The oxidant is required to diffuse through the gas film boundary layer and the ash layer. The ash in the AS model is assumed to crumble and fall away from the char particle with the oxidant required to diffuse only through the gas film boundary layer. An ash layer may collect around the particle during oxidation as observed during the burning of large coal slabs (Park and Edgar, 1987).

The char oxidation/gasification submodels assume global reactions and depend on the external particle surface area. The SP or AS submodels are used to obtain the rates of char oxidation and gasification. Derivation of the rate equation for a single particle is given by Hobbs (1990):

$$r_i^{o,g} = \frac{A_p \nu_s M w_p C_{ig}}{\frac{1}{k_r \zeta} + \frac{1}{k_m} + \frac{1}{k_{\text{eff}}}} \tag{8}$$

The resistances in the denominator represent surface reaction, molecular diffusion through the gaseous film and diffusion through the ash layer. Equation 8 neglects the effects of diffusion-induced convective transport and assumes that the reactions are first order in oxidizer concentration. The validity of Eq. 8 has not been demonstrated for groups or packed beds of oxidizing particles. Values obtained for reaction order among various investigators vary between 0 and 1, with most investigators correlating their data on the basis of first order. Gray et al. (1974) explain the variation in terms of the controlling chemical reaction step: if adsorption is controlling, $n=1$, whereas if desorption controls, $n=0$, where n is the order of the reaction.

Equation 8 also explicitly neglects pore diffusion, in which case these effects are lumped into k_{eff}. The diffusional resistance through the ash layer is set to zero if the AS model is used. Oxidation and gasification kinetic rate constants are given in Table 4. Given the lack of more reliable steam-char reaction rate data, it has been assumed, based on the data of Walker (1959), Yoon (1978), Wen et al. (1982), Wen and Chaung (1979), and Blackwood (1959), that the steam gasification rate is the same as the carbon dioxide gasification rate: $A_{H_2O} = A_{CO_2}$, and $E_{H_2O} = E_{CO_2}$. Based on the same references, the hydrogen gasification rate is taken to be three orders of magnitude smaller than the carbon dioxide rate: $A_{H_2} = 10^{-3} A_{CO_2}$ and $E_{H_2} = E_{CO_2}$. Although the parameters in Table 4 were derived from small-particle experimentation, the kinetic rate constants are assumed to be applicable to large-particle oxidation and gasification. Large-particle oxidation and gasification data are scarce. The model uses measured char oxidation rate data for various coals correlated to first-order kinetics, Table 4. Acceptable predictions can be obtained with these correlations without a precise knowledge of the mechanism or the intrinsic reaction order. This is particularly effective when correlated rates are for the same or similar coal of the appropriate size covering the appropriate temperature range. Use of this simpler expression makes the addition of important diffusional effects more straightforward.

Several studies have been done on large spherical carbon particles (for example, Froberg, 1967; Kurylko, 1969) and may not be applicable to coal. Mass transport, however, may dominate the oxidation and gasification processes. For example, diffusion through an ash layer was shown to be significant when predicting burning rates for large coal slabs (see Hobbs, 1990). For the slab, the film resistance was 10 orders of magnitude higher than the chemical resistance for oxidation using the parameters in Table 4. Similar results were obtained from the large particle rates of Froberg (1967) and Kurylko (1969). Although chemical rates for small particles may differ from large particle rates, film diffusion and internal diffusion dominate, at least for oxidation. Additional experimental data are needed to make this same conclusion for the gasification reactions.

The last resistance in the denominator of Eq. 8 can be determined using an effective mass-transfer coefficient (Thorsness and Kang, 1984):

$$\frac{1}{k_{\text{eff}}} = \frac{(1-F)d_p}{2D_{\text{eff}}} \tag{9}$$

Walker et al. (1959) and Laurendeau (1978) discuss methods for calculating effective diffusivities. Park and Edgar (1987) show the effect of a developing ash layer on the burning rate of a core sample of coal. The core burning rate can be predicted by using an effective diffusivity based on the molecular diffusivity multiplied by a constant ($D_{\text{eff}} = \phi D_{im}$). The molecular diffusivity, D_{im}, was calculated from Chapman-Enskog theory for gas mixtures (Bird et al., 1960). The constant, ϕ, is based on the porosity of the developing ash layer. Thorsness and Kang (1985) have used 0.35 for ϕ. Wang and Wen (1972) have measured porosity of a fire clay ash which varied from 0.4 to 0.8. Laurendeau (1978) shows that ϕ can be estimated by the ash porosity divided by the tortuosity, which was taken to be 2. Using Wang and Wen's values for the ash porosity (0.4 to 0.8), ϕ should range between 0.2 and 0.4. However, lower values of ash porosity were determined for ash originating

Table 4. Oxidation and Gasification Kinetic Rate Constants (after Hedman et al., 1987)*

		$k_r = A_r T \exp(-E_r/RT)$, m/s			
Reaction	Rank	A_r, m/s·K	E_r/R, K	Source of Data	Source of Correlation
$C + 0.5\ O_2 \rightarrow CO$	All ranks*	2.30	11,100	Field et al. (1967)	Baxter (1987)**
	HVBA	1.03	9,010	Goetz et al. (1982)	Baxter (1987)
	HVBC	0.50	6,310	Goetz et al. (1982)	Baxter (1987)
	SUBC	10.4	11,200	Goetz et al. (1982)	Baxter (1987)
	Lignite A	1.22	10,300	Nsakala et al. (1985)	Nsakala et al. (1985)
$C + CO_2 \rightarrow 2\ CO$	All ranks*	589.0	26,800	Goetz et al. (1982)	This study†
	HVBA	1,160.0	31,200	Goetz et al. (1982)	Baxter (1987)
	HVBC	4,890.0	31.300	Goetz et al. (1982)	Baxter (1987)
	SUBC	6,190.0	28,900	Goetz et al. (1982)	Baxter (1987)
	Lignite A	3.42	15,600	Goetz et al. (1982)	Baxter (1987)

*Base case parameters used in sensitivity analysis.
**Baxter's (1987) rate constants were obtained by nonlinear analysis of Field et al. (1967) and Goetz (1982) data.
†The CO_2 rate constants for all ranks were obtained in this study by averaging Baxter's (1987) rate constants for four coal ranks.

from the Lurgi and Wellman-Galusha gasifiers (Hobbs, 1990). Porosities for these ashes ranged from 0.06 to 0.60, indicating a lower range for ϕ of 0.03 to 0.3 for fixed-bed gasifiers.

The single-particle model can be related to the bed by using particle number density and the unreacted core particle surface area. The particle diameter, unreacted core diameter, and number density for the SP model were obtained by mass balance, assuming spherical particles and constant solids density:

$$d_p = [(1-\Omega^o_{\text{ash}})d_u^3 + \Omega^o_{\text{ash}} d_o^3]^{1/3} \tag{10}$$

$$d_u = F^{1/3} d_o \tag{11}$$

$$\eta_p = \frac{6(1-\epsilon)}{\pi d_p^3} \tag{12}$$

The heterogeneous oxidation of carbon produces both CO and CO_2 as primary products as shown in the following reaction:

$$\lambda C + O_2 \rightarrow 2(\lambda - 1)CO + (2-\lambda)CO_2, \quad 1 \le \lambda \le 2 \tag{13}$$

Carbon monoxide may be favored at higher temperatures, if CO is formed at carbon edges and CO_2 is formed at inorganic sites. Lower temperatures may favor CO_2 due to catalytic activity. The CO/CO_2 ratio has been correlated by Laurendeau (1978):

$$\frac{CO}{CO_2} = A\exp\left(-\frac{E}{RT}\right) = \frac{2(\lambda-1)}{(2-\lambda)} \tag{14}$$

where $A \approx 10^{2.5}$ and $E \approx 25$–38 kJ/mol for low pressures, and $A \approx 10^{3.5}$ and $E \approx 50$–80 kJ/mol at high pressures. The stoichiometric coefficient for Eq. 13 can be determined as a function of temperature from Eq. 14:

$$\lambda = \frac{2\left[A\exp\left(-\frac{E}{RT}\right)+1\right]}{A\exp\left(-\frac{E}{RT}\right)+2} \tag{15}$$

For oxidation, λ is equal to ν_s in Eq. 8. Values for λ at 500, 1,000, 1,500 and 2,000 K are 1.08, 1.78, 1.93, and 1.96, respectively, using Eq. 15 with the low-pressure parameters; 1.00, 1.06, 1.47, and 1.76, respectively, using the high-pressure parameters. Thus, CO is favored at higher temperatures.

Model equations, options and parameters

The one-dimensional fixed-bed model equations are summarized in Table 5. The 38 ordinary differential equations in Table 1 were solved simultaneously from the top to the bottom of the reactor with LSODE (Livermore Solver for Ordinary Differential Equations, Hindmarsh, 1983). Drying, devolatilization, combustion, and gasification are described by Eqs. 4, 5 and 8. The volumetric heat-transfer rates from solid to gas, solid to wall, and gas to wall are described by Eqs. 1, 2 and 3. The heat- and mass-transfer correlations are in Table 2.

Table 5. Summary of the One-Dimensional Fixed-Bed Model Equations

Basic Equations and Boundary Conditions	Reference
Overall gas species continuity	Table 1
Overall solid species continuity	Table 1
Gas-phase energy	Table 1
Solid-phase energy	Table 1
Solid species continuity	Table 1
Gas-phase elemental continuity	Table 1
Gas-phase tar species continuity	Table 1
Gas-phase tar elemental continuity	Table 1
Auxiliary Equations	**Reference**
Ash heat capacity	Mills and Rhine (1989)
Devolatilization rates	Eqs. 5 and 6
Diffusive radiation coefficients	Table 2
Drying rate	Eq. 4
Effective gas and solid conductivities	Table 2
Enthalpy exchange due to reaction	Hobbs (1990)
Formation enthalpies	Hobbs et al. (1992)
Gas conductivity, viscosity, and diffusivity	Bird, et al. (1960)
Gas-to-wall heat-transfer coefficient	Table 2
Mass-transfer coefficient	Table 2
Oxidation and gasification rates	Eq. 8
Particle diameter and surface area	Hobbs (1990)
Particle number density	Eq. 12
Pressure drop	Ergun (1952)
Reynolds, Prandl and Schmidt numbers	Table 2
Sensible enthalpies	Hobbs et al. (1992)
Solid conductivity	Table 2
Solid-to-gas heat-transfer coefficient	Table 2
Solid-to-wall heat-transfer coefficient	Table 2
Total enthalpies	Hobb et al. (1992)
Volumetric solid-to-gas heat-transfer rate	Eq. 1
Volumetric wall heat loss from gas	Eq. 2
Volumetric wall heat loss from solid	Eq. 3

Elemental reaction rates can be determined from reaction stoichiometry. The tar reaction rates can be determined from Eq. 6.

The one-dimensional fixed-bed model parameters and options are summarized in Table 6. Parameters that are difficult to obtain and subject to the most uncertainty include the solid-to-gas heat-transfer coefficient, effective diffusivity, and bed void fraction. It has been reported (Lowry, 1963) that the solid-to-gas heat-transfer coefficient typically ranges between 0.02 and 0.1 times that for a nonreacting fixed-bed system; this is discussed in detail in the sensitivity analysis. The effective diffusivity can be estimated from measured ash porosity. Bed void fraction for the feed coal can also be determined experimentally. However, the bed void fraction is not constant throughout the reactor. Values at the top and bottom of the reactor are required in the one-dimensional model.

Solution technique

The set of equations in Table 5 with boundary conditions describes a split boundary value problem. The term "split boundary" has been used to describe the partially known and unknown boundary conditions at both the top and the bottom of the moving-bed reactor. Although split boundary value problems have been solved satisfactorily for homogeneous models (equal solid and gas temperatures), heterogeneous models are more difficult to solve. For example, converged results from Cho's heterogeneous model (1980) indicate that the solid temperature is close to the gas temperature at the top

Table 6. Summary of One-Dimensional Fixed-Bed Model Parameters and Options

Parameter	Typical Value (Source)	Description
Devolatilization		
x^o	0.110–0.270 (Table 3)	Potential tar-forming fraction
k_i^o 1/s	0.81×10^{13} (CO_2 extra loose; Serio et al., 1987)	Functional group frequency factor
E_i/R, K	22,500 (CO_2 extra loose; Serio et al., 1987)	Functional group activation energy
k_x^o, 1/s	0.86×10^{15} (Tar; Serio et al., 1987)	Tar frequency factor
E_x/R, K	27,700 (Tar; Serio et al., 1987)	Tar activation energy
Oxidation/Gasification		
A_{CO_2}, m/s·K	589.0 (Table 4)	Gasification frequency factor
E_{CO_2}/R, K	26,800 (Table 4)	Gasification activation energy
A_{H_2}, m/s·K	0.589 (Table 4)	Gasification frequency factor
E_{H_2}/R, K	26,800 (Table 4)	Gasification activation energy
A_{H_2O}, m/s·K	589.0 (Table 4)	Gasification frequency factor
E_{H_2O}/R, K	26,800 (Table 4)	Gasification activation energy
A_{O_2}, m/sK	2.30 (Table 4)	Oxidation frequency factor
E_{O_2}/R, K	11,100 (Table 4)	Oxidation activation energy
Flow, Heat and Mass Transport		
ϵ'	0.85 (Table 2)	Coal emissivity
ϵ top	0.23–0.40 (Table 7)	Bed void at bed top
ϵ bottom	0.33–0.67 (Table 7)	Bed void at bed bottom
ζ	0.10 (Lowry, 1963)	Reactive/nonreactive heat-transfer coeff.
ϕ/τ^2	0.50 (Laurendeau, 1978)	Ash porosity divided by tortuosity squared
Operating Parameters		
Prox. & ult.	Table 7	Proximate and ultimate analysis
d_p, cm	1.27–3.63 (Table 7)	Particle diameter
D, m	1.98–2.74 (Table 7)	Reactor inside diameter
z, m	1.83–3.05 (Table 7)	Bed height
P, kPa	100–2,600 (Table 7)	Reactor pressure
T_{coal}, K	298 (Table 7)	Inlet coal temperature
T_{BG}, K	331–644 (Table 7)	Feed gas temperature
T_{wall}, K	310–498 (Table 7)	Wall temperature
m_c, kg/s	0.179–2.23 (Table 7)	Coal mass-flow rate
m_o, kg/s	0.335–0.948 (Table 7)	Oxidizer mass-flow rate
m_s, kg/s	0.0500–2.80 (Table 7)	Steam mass-flow rate
Model Options		
(1) AS or SP char submodel; (2) gas-phase tar reaction equilibrium option; (3) volatiles mass-transport option; (4) combustion product distribution.		

of the reactor, which was 1,050 K. However, the initial temperature of the solid at the top of the reactor was specified to be 370 K. In this study, iterative methods were used to satisfy temperature boundary conditions.

A two-zone, well-mixed, equilibrium-based, fixed-bed model (Hobbs et al., 1992) has been used here to provide an initial estimate of the effluent gas composition and temperature. However, the gas exit temperature predicted by the two-zone model is generally high due to the assumption that the devolatilization zone is at a single temperature. Likewise, the exit solid temperature is high due to the well-mixed assumption. Thus, after integrating from the top to the bottom of the reactor, the calculated feed gas temperature will be higher than the input feed gas temperature. Therefore, a new exit gas temperature must be estimated which is smaller than the temperature predicted by the two-zone model. This procedure can be repeated in an iterative manner until the calculated feed gas temperature is equal to the input feed gas temperature. In general, burnout should also be used as an iteration variable. However, burnout is typically high in fixed-bed gasifiers, and thus it was assumed to be unity for all calculations reported here and was not used as an iteration variable. Iterations using temperature converged to a burnout equal to unity. Typically, two to four iterations through the gasifier are required for convergence. Hobbs (1990) provides details on the computational algorithm. Calculation times for one sweep through the reactor using an engineering workstation for the two-zone model and one-dimensional model are on the order of seconds and minutes, respectively.

Parametric Analysis

The parametric sensitivity analysis was divided into three major categories: model options, model parameters, and operational parameters. Four model options were investigated: tar vapor reaction equilibrium, volatiles mass transport, char ash layer formation and combustion product distribution. Seven model parameters were also examined: solid-to-gas heat-transfer coefficient, effective diffusivity, bed-to-wall heat-transfer coefficient, potential tar-forming fraction, functional group composition, coal density, and oxidation and gasification kinetic parameters. Furthermore, eight operational parameters were examined: feed gas temperature, reactor pressure, coal mass flow rate, steam mass flow rate, air mass flow rate, proximate ash content of the feed coal, coal particle diameter, and bed void fraction.

The response to parametric changes in input parameters can be observed in various output parameters such as solid temperature, gas temperature, gas concentrations, and pressure drop. Solid temperature was chosen as the primary response variable for all the parametric simulations, since it is indicative of the extent of heterogeneous reaction. The base case for the parametric sensitivity simulations was gasification of Jetson bituminous coal in an air-blown Wellman-Galusha gasifier

Table 7. Operating Parameters for Lurgi and Wellman-Galusha Gasifiers

Gasifier*	Lurgi	WG	WG	WG	WG	WG	WG	WG	WG
Coal Type	Rosebud Subbitum.	Absaloka Subbitum.	Benton Lignite	Elkhorn Bituminous	Jetson Bituminous	Kemmerer Subbitum.	Leucite Subbitum.	Rosebud Subbitum.	Utah B.C. Bituminous
Proximate, wt. %									
Ash	9.7	6.3	6.4	4.7	4.3	5.7	9.0	11.8	11.1
Fixed carbon	36.4	40.7	25.9	53.7	49.5	42.4	44.9	40.1	43.9
Moisture	24.7	23.5	32.8	4.6	6.3	16.8	17.4	21.3	6.1
Volatile	9.2	29.6	34.9	36.9	39.9	35.1	28.8	26.8	38.9
Ultimate, wt. %									
Carbon	77.1	76.3	73.7	82.5	81.4	77.5	78.1	78.7	80.3
Hydrogen	4.9	5.1	6.2	5.7	5.1	5.6	5.0	4.9	6.2
Nitrogen	1.4	0.8	1.0	1.6	1.8	1.2	1.9	1.1	1.2
Sulfur	1.7	0.4	0.9	0.9	1.6	1.0	0.6	1.3	0.6
Oxygen	15.0	17.4	18.2	9.3	10.2	14.7	14.4	14.0	11.7
Operating Parameters									
Chamber inside dia., m	2.74	1.98	1.98	1.98	1.98	1.98	1.98	1.98	1.98
Bed Height, m	3.05	2.11	2.13	2.13	1.83	2.13	2.00	2.00	2.13
Chamber pres., kPa	2,560	101.3	101.3	101.3	101.3	101.3	101.3	101.3	101.3
Apparent density, kg/m^3	1,270	1,260	1,200	1,300	1,190	1,260	1,310	1,310	1,220
Particle dia., cm	1.61	2.29	3.05	3.63	2.03	1.27	2.54	2.29	2.16
Void fraction at bed top**	0.40	0.36	0.25	0.35	0.33	0.30	0.32	0.23	0.33
Void fraction at bed bottom**	0.50	0.50	0.45	0.46	0.60	0.52	0.46	0.33	0.67
Inlet coal temp., K	298	298	298	298	298	298	298	298	298
Feed gas temp., K	644	332	340	331	334	332	334	336	335
Wall temp., K	498	310	310	310	310	310	310	310	310
Coal mass flow, kg/s	2.23	0.420	0.749	0.324	0.352	0.284	0.293	0.179	0.337
Air-mass flow, kg/s†	0.58	0.764	0.931	0.789	0.948	0.573	0.532	0.335	0.673
Steam mass flow, kg/s	2.80	0.114	0.231	0.113	0.156	0.0881	0.0883	0.050	0.119
Jacket steam mass flow, kg/s	0.31	0.0034	0.051	0.0082	0.134	0.0030	0.0620	0.0174	0.0261
Wall heat loss, MW‡	0.836	0.155	0.226	0.260	0.416	0.167	0.291	0.169	0.295
Wall heat loss, MW§	0.888	0.343	0.481	0.518	0.257	0.197	0.255	0.126	0.341
Reference¶		12 (53)	10 (55)	9 (71)	2 (68)	14 (49)	4 (59)	15 (50)	13 (57)

*WG represents the atmospheric Wellman-Galusha Gasifier.
**Estimated from measured bulk and apparent densities.
†Oxygen mass-flow rate for the Lurgi case, kg/s.
‡Heat loss calculated from reported jacket steam and cooling water heat loss.
§Heat loss calculated with the one-dimensional model (MBED-1D).
¶Volume (underlined) and page number (in parenthesis) of Thimsen et al. (1984).

(Thimsen et al., 1984). Operational data for the Jetson case are given in Table 7. Additional parameters required by the one-dimensional model for the base case (Jetson) are given in Table 3. The sensitivity of temperature to the solid-to-gas heat-transfer coefficient was completed for eight different cases, rather than just the Jetson case. Input parameters for these eight cases are also reported in Table 7.

Model options

Tar Vapor Chemistry. The one-dimensional, fixed-bed model has two options for treating tar vapor chemistry: 1. the tar is allowed to react in the gas phase to completion (chemical equilibrium assumption); or 2. the tar vapor is nonreactive (in thermal equilibrium, but "frozen" chemically). Condensed-phase tar remaining in the solid is considered as part of the char. If option 1 is chosen, all gases including tar are assumed to be in chemical equilibrium. If option 2 is chosen, all gases except for tar are assumed to be in chemical equilibrium.

The predicted sensitivity of the axial solid temperature profile to the tar gas-phase equilibrium assumption for gasification of Jetson bituminous coal in an atmospheric, air-blown, Wellman-Galusha gasifier is shown in Figure 3A. Use of the equilibrium assumption caused a small shift in the temperature peak toward the bottom of the reactor. This small effect can be explained by noting that gasifiers operate fuel-rich near the top of the gasifier. When the tar reacted to equilibrium in the drying and devolatilization zones, the gas phase became more fuel-rich, which caused the temperature to decrease slightly. The decrease in temperature in the devolatilization zone caused the devolatilization zone length to increase, which consequently caused the entire temperature profile to shift toward the reactor bottom. The transition between the devolatilization zone and the gasification zone was more gradual when the tar was allowed to react to equilibrium. Again, the gradual transition was caused by lower temperatures.

Volatiles Mass Transport. The predicted sensitivity of axial solid temperatures to the devolatilization mass transport (Eq. 7) for gasification of Jetson bituminous coal in an atmospheric, air-blown Wellman-Galusha gasifier is shown in Figure 3B. Inclusion of mass-transport resistance caused only a small effect on the solid temperature profile. The more rapid release of volatile matter near the reactor top caused the gas phase to become fuel-richer, which consequently caused the temperature of the devolatilization zone to decrease. The decreased temperature in the devolatilization zone caused the devolatilization zone length to increase, which caused the location of the maximum temperature to move toward the bottom of the reactor.

Char Ash Layer. The predicted sensitivity of axial solid temperature to the SP and AS ash assumptions for gasification

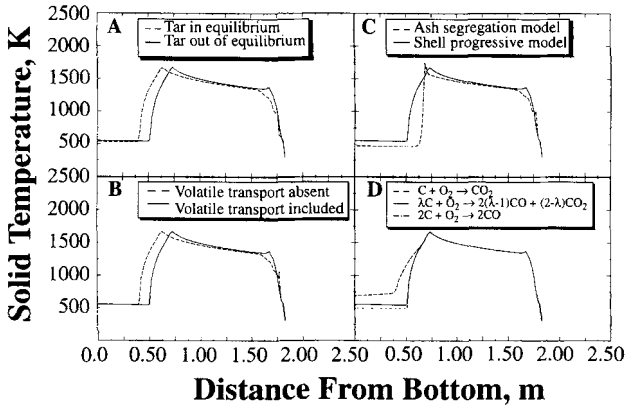

Figure 3. Predicted sensitivity of axial solid temperature to model options: A) tar gas-phase equilibrium assumption; B) volatile mass-transport assumption; C) char model ash assumption; and D) distribution of CO and CO_2 for the char oxidation reaction.

Simulation is for gasification of Jetson bituminous coal in an air-blown Wellman-Galusha gasifier. Input parameters are in Tables 3, 4, 7 and 8.

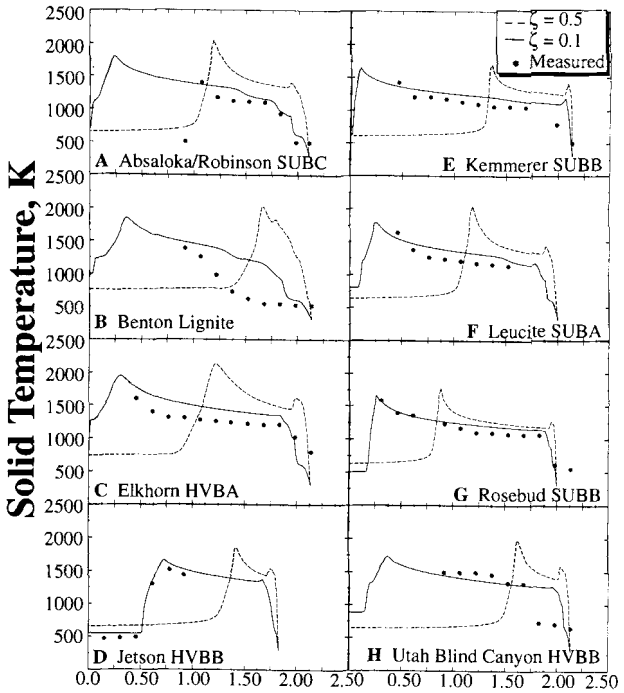

Figure 4. Predicted sensitivity of axial solid temperature to solid-to-gas heat-transfer correction factor, ζ, in an atmospheric pressure Wellman-Galusha gasifier fired with: A) Absaloka/Robinson subbituminous; B) Benton lignite; C) Elkhorn bituminous; D) Jetson bituminous; E) Kemmerer subbituminous, F) Leucite subbituminous; G) Rosebud subbituminous; and H) Utah Blind Canyon bituminous coals.

Measurements from Thimson et al. (1984). Input conditions are given in Tables 3, 4, 7 and 8.

of Jetson bituminous coal in an atmospheric air-blown Wellman-Galusha gasifier is shown in Figure 3C. Once again, relatively small differences are observed between the two options. The shape of the solid temperature profile using the AS model (no ash layer) was sharper than the broad peak predicted by the SP model. Also, the maximum temperature was higher when the AS model option was chosen. The two char models represent extremes in ash behavior, although the SP model may be closer to actual ash behavior. This observation is based on 1) comparing predicted temperature profiles to measured temperature profiles and 2) experimental observations of large-particle oxidation which show ash-layer accumulation (Park and Edgar, 1987). However, more specific data on oxidation of large particles in packed beds is required to confirm this suggestion.

Use of the AS submodel option resulted in an increased rate of carbon being added to the gas phase, which caused the gas phase to become fuel-richer. In the drying, devolatilization and gasification zones, a decrease in temperature was calculated. The combined effects of a shorter oxidation zone due to more rapid reaction and a lower devolatilization zone temperature caused the location of the maximum temperature to remain nearly unchanged.

Oxidation Product Distribution. Predicted sensitivity of axial solid temperature and gas concentration to the distribution of combustion products CO and CO_2 during gasification of Jetson bituminous coal in an atmospheric, air-blown Wellman-Galusha gasifier is shown in Figure 3D. Three assumptions are shown: 1) CO_2 as the sole primary combustion product; 2) CO as the sole primary combustion product; and 3) a distribution of CO_2 and CO combustion products that depends on solid temperature (Eq. 14). As expected, only the oxidation zone was affected by the combustion product distribution assumption. Different temperatures resulted from the energy exchange at the particle-to-gas interface due to reaction. Close agreement between the sole CO distribution and the combined CO/CO_2 distribution suggests that carbon monoxide may be assumed to be the primary product at typical combustion temperatures, which complements the findings of Laurendeau (1978).

Model parameters

Solid-to-Gas Heat-Transfer Coefficient. Effects of key model parameters that have not been reported experimentally and have a significant impact on the solid temperature profile were investigated. The solid-to-gas heat-transfer coefficient for a nonreacting system may be 10 to 50 times higher ($\zeta = 0.02$–0.1) than that for a reacting system (Lowry, 1963). Dzhaphyev et al. (1986) attribute the observed difference to unsteady heat transfer. Vigorous reactions as well as nonsphericity and transpiration cooling may also contribute to this difference. The solid temperature is sensitive to this ratio, ζ. Predicted sensitivity of axial solid temperature to ζ for the Wellman-Galusha cases is shown in Figure 4, where measured temperatures are also shown. None of the measured and predicted profiles correspond when ζ is greater than 0.1. All profiles in Figure 4

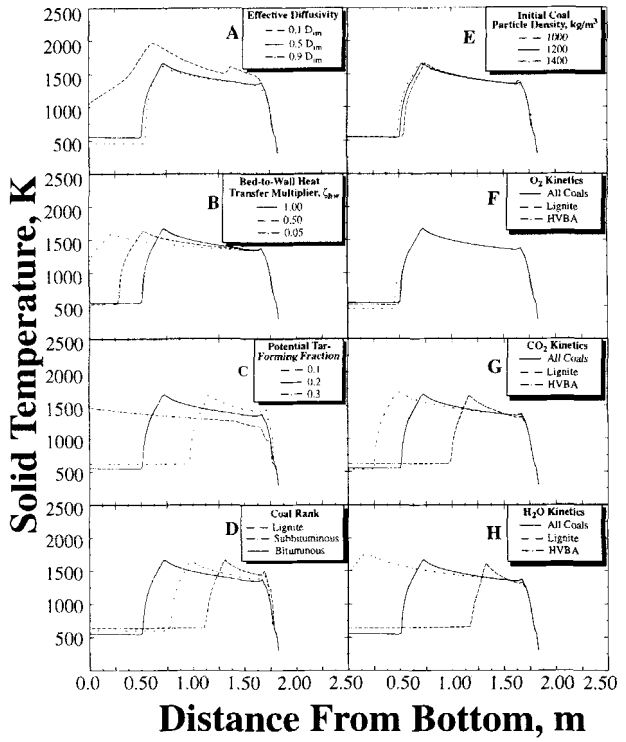

Figure 5. Predicted sensitivity of axial solid temperature to model parameters; A) effective diffusivity; B) bed-to-wall heat transfer; C) potential tar-forming fraction; D) coal rank; E) initial coal particle density; F) O_2-char oxidation kinetic parameters; G) CO_2-char gasification kinetic parameters; and H) H_2O-char gasification kinetics.

Input conditions are for atmospheric gasification of Jetson bituminous coal in an air-blown Wellman-Galusha gasifier. Input conditions are in Tables 3, 4, 7 and 8.

also show the importance of treating devolatilization as a kinetic process. The Benton lignite case with 33% moisture shows that the drying zone was about 0.5 m, thus discounting the common assumption of instantaneous drying.

Effective Diffusivity. The predicted sensitivity of the solid temperature to the effective diffusivity (Eq. 9) is shown in Figure 5A. The effective diffusivity affects the location of the maximum solid temperature, the magnitude of the maximum solid temperature, and the shape of the solid temperature profile. Lower values of ϕ (D_{eff}/D_{im}) cause the location of the maximum solid temperature to shift toward the bottom of the reactor and the size of the oxidation zone to increase, because the char oxidizes more slowly.

Bed-to-Wall Heat Transfer. The sensitivity of solid temperature to the bed-to-wall heat-transfer coefficient is shown in Figure 5B. For the calculations, h_w from Eq. 1 in Table 2 was multiplied by a constant, ζ_{hw}, to see the effect of lowering bed-to-wall heat transfer. Lower values of ζ_{hw} caused the solid temperature to decrease in the gasification and oxidation regions of the gasifier. The shift in location of the maximum solid temperature and the change in the shape of the curve were attributed to a redistribution of solid enthalpy.

Tar Fraction. Predicted sensitivity of solid temperature to the potential tar-forming fraction, x^o (maximum tar yield), for the base case is shown in Figure 5C. To provide a consistent method of calculating tar, a semi-empirical model of Ko et al. (1988) was used to predict tar yield. As x^o was increased, the ultimate volatile yield also increased and the corresponding ultimate char yield decreased, which resulted in a smaller gasification/oxidation zone. The shift in the location of the maximum solid temperature was attributed to the smaller oxidation and gasification zones.

Coal Rank. The predicted sensitivity of solid temperature to coal rank is shown in Figure 5D. Three different coal types were investigated: lignite, subbituminous, and bituminous coals. The solid temperature sensivity to rank may be attributed to the rank dependence of volatile matter (that is, lower-rank coals contain more volatile matter than higher rank coals). The increase in ultimate volatile yield and corresponding decrease in ultimate char yield resulted in a smaller gasification/oxidation zone.

Coal Density. During devolatilization, coal particles evolve tars and gases, and the density can decline. The particles can also soften and swell depending on coal rank. Thus, it is expected that solids density will decline during devolatilization. The rate equations for devolatilization (Eqs. 5 and 6) depend on initial coal density which is specified. However, rates of char reaction (with O_2, CO_2, H_2O, and H_2) depend on the char density, not on the original coal density. Further, the char density can change during oxidation (Smith, 1983). In this study, the solid density was taken to be constant throughout the bed at the initial coal density value. Sensitivity of solids density was tested by comparing temperature and pressure with different initial solids density values of 1,000-1,400 kg/m^3. Effects of solid density are shown in Figure 5E to be modest.

Oxidation and Gasification Kinetics. Sensitivity of solid temperature to oxidation and gasification parameters (Table 4) is shown in Figures 5F through 5H. The solid temperature was not sensitive to the H_2 gasification kinetics because of the slow reaction rate and is therefore not shown. The solid temperature, however, was sensitive to the O_2, CO_2 and H_2O gasification kinetic parameters as shown in Figures 5F and 5H. Differences among coals were small for oxygen rates, but large for CO_2 and H_2O rates, with faster rates shortening the gasification zone. This suggests that reliable gasification rates for specific coals are required to make reliable predictions.

Operational parameters

Sensitivity of solid temperature to operational parameters is shown in Figure 6. Operational parameters that can be changed readily are the feed gas temperature, the reactor pressure, the coal mass-flow rate, the steam mass-flow rate, and the air-mass-flow rate. Other operational parameters are not as easily modified during daily operation. Such parameters include the proximate ash content, coal particle diameter, and the bed void fraction. Coal selection or pretreatment such as washing or crushing may be necessary to change these parameters.

Feed Gas Temperature. The location and magnitude of the maximum solid temperature were substantially affected by feed gas temperature (Figure 6A). As expected, the maximum temperature decreased when feed gas temperature was lowered, while the location of the maximum temperature at steady operating conditions shifted toward the bottom of the reactor.

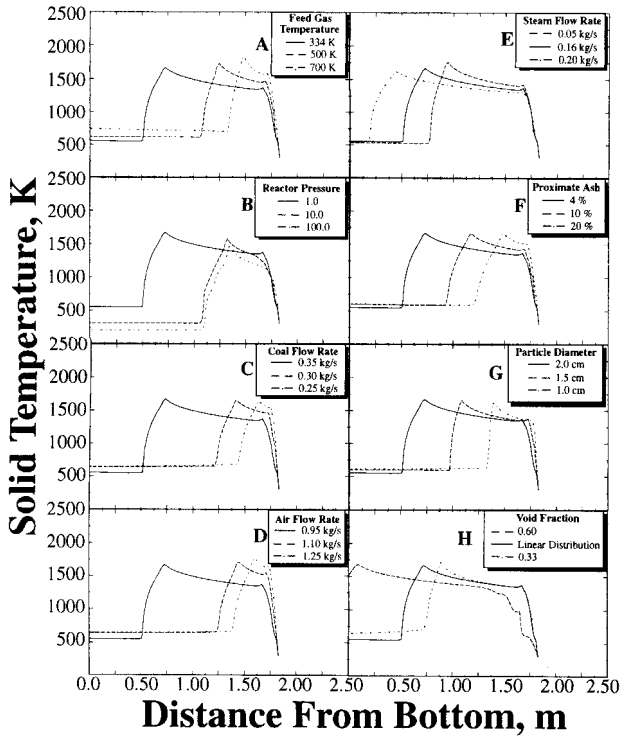

Figure 6. Predicted sensitivity of axial solid temperature to operational variables: A) feed gas temperature; B) reactor pressure; C) feed coal mass-flow rate; D) feed air-mass-flow rate; E) feed steam mass-flow rate; F) feed coal proximate ash content; G) feed coal mean particle diameter; and H) bed void fraction.

Input conditions are for atmospheric gasification of Jetson bituminous coal in an air-blown Wellman-Galusha gasifier. Input conditions are in Tables 3, 4, 7 and 8.

The lower feed gas temperature caused the effluent gas temperature to decrease. The lengths of the drying, the devolatilization, the gasification, and the oxidation zones were all increased, which caused the location of the maximum temperature to move toward the bottom of the reactor.

Reactor Pressure. The predicted sensitivity of solid temperature to reactor pressure is shown in Figure 6B. Increasing pressure at lower pressure levels caused the location of the maximum temperature to shift toward the top of the reactor. The change in temperature gradient in the oxidation zone of the high-pressure simulation was due to competition between the highly exothermic oxidation reaction and the endothermic steam gasification reaction. This effect was substantial in the high-pressure Lurgi case discussed subsequently. Once the solid temperature is sufficiently high for the oxidation reaction to begin, the rapid oxidation of carbon causes the solid temperature to increase dramatically. Once the temperature reaches about 1,000 K, the steam reaction begins. Although the steam reaction is not as fast as the oxidation reaction, the concentration of steam is significantly higher than the oxygen concentration. Thus, carbon consumption associated with the steam reaction approaches the carbon consumption associated with the oxidation reaction. The endothermic steam gasification reaction quenches the rapid increase in solid temperature and causes a sudden change in solid temperature, which was observed in the high-pressure case in Figure 6B.

When pressure is increased, the partial pressure of the water increases. Although the partial pressure of oxygen is also increased, the greater abundance of steam causes a substantial increase in the steam gasification reaction. The effect is to magnify the competition between the endothermic and exothermic reactions, producing a small peak shown subsequently in Figure 7A. Also, the diffusivity of water is greater than that of oxygen. Therefore, the steam gasification reaction is amplified at higher pressures.

Coal Flow Rate. The predicted sensitivity of solid temperature to coal mass-flow rate is shown in Figure 6C. All parameters in these simulations were held constant except for the coal mass-flow rate. The substantial shift in the location of the maximum temperature profile was attributed to a decrease in time required to consume all of the organic matter in the coal. The low coal mass-flow rates correspond to combustion occurring at the top of the gasifier. Thus, both combustion and gasification runs are depicted in Figure 6C.

Air Flow Rate. The predicted sensitivity of solid temperature to air-mass-flow rate is shown in Figure 6D. The influence of air-mass-flow rate was similar to that of coal mass flow rate. Again, the higher air-mass-flow rate corresponded to a combustion case. The shift in location of the maximum temperature was attributed to increased oxidation rates.

Steam Flow Rate. The predicted sensitivity of the solid temperature to the steam mass-flow rate is shown in Figure 6E. As the steam mass-flow rate was increased, both the lo-

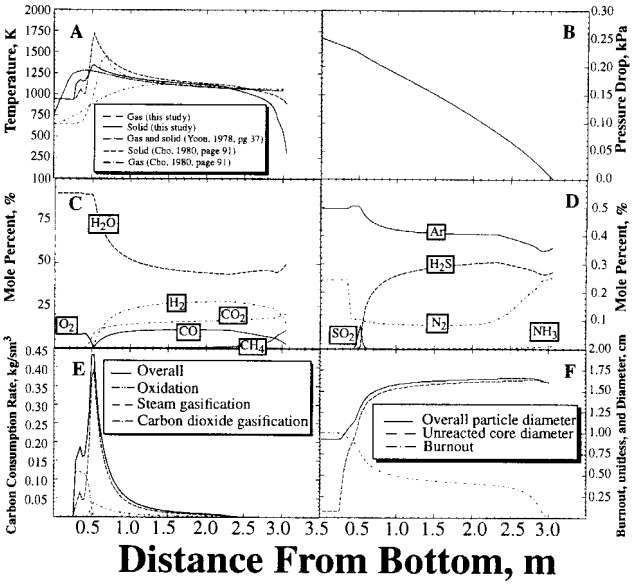

Figure 7. Predicted axial: A) temperature; B) pressure drop; C) major species concentration; D) minor species concentration; E) oxidation/gasification carbon consumption rate; F) burnout, overall and unreacted particle diameter in a high-pressure, oxygen-blown Lurgi gasifier fired with Rosebud subbituminous coal.

Input parameters are in Tables 3, 4, 7 and 8. Figure A shows results from the homogeneous model of Yoon (1979) and the heterogeneous model of Cho (1980).

cation and the magnitude of the maximum temperature were affected. Increasing feed steam caused the maximum temperature to decrease. The shift in the location of the maximum temperature is caused by lower exit temperatures associated with higher steam mass-flow rates. This operational parameter is used frequently to control the temperature to avoid significant ash melting.

Ash Content. The predicted sensitivity of solid temperature to proximate ash content of the feed coal is shown in Figure 6F. The shift in the location of the maximum solid temperature is analogous to the temperature shift caused by the coal mass-flow rate. Lower proximate ash content is equivalent to an increase in the coal mass-flow rate, which results in a larger gasification zone. Similar results were obtained when the proximate moisture content was changed.

Particle Diameter. The predicted sensitivity of solid temperature to feed coal particle diameter is shown in Figure 6G. Small particles heat up faster and react sooner than large particles. The increased solid temperature promotes all reactions, which are completed much earlier for the smaller particles than for the larger particles. Also, mass transport resistances are less for small particles than for large particles. Particle-size effects are approximately linear as shown in Figure 6G. The influence of a distribution of particle sizes is more difficult to determine. Heat- and mass-transport rates are affected significantly, and the bed void fraction may also change dramatically, as discussed in the following section. Wide particle-size distributions tend to decrease the bed void fraction (Fayed and Otten, 1984).

Void Fraction. The predicted sensitivity of solid temperature to bed void fraction is shown in Figure 6H. The void fraction significantly affects the particle number density, which in turn affects the overall bed consumption rate. Increasing void fraction causes a decrease in the overall bed reaction rate. Drying, devolatilization, gasification and oxidation rates are all decreased significantly when the void fraction is increased. Thus, all prominent reaction zones increase with increasing bed void fraction, and the location of the maximum temperature moves toward the bottom of the reactor.

Rapid increase in the solid temperature at the reactor top is due, for the most part, to the rising hot gases from the oxidation zone heating the descending coal particles. The solid heat capacity is reduced significantly by the release of the volatiles in the devolatilization zone making the solid temperature increase more rapidly. The gas temperature, at the same time, is reduced sharply due to the mixing with colder volatiles released from the solids.

Model parameters with the most uncertainty are the solid-to-gas heat-transfer coefficient and the effective diffusivity coefficient. Methods used for estimates of these parameters are summarized in Table 8. If experimental values are unavailable, the approach of Table 8 can be used with caution to estimate bed void fraction, ϵ, solid-to-gas heat-transfer ratio, ζ, and the ash porosity, ϕ, and consequently, the effective diffusivity.

Table 8. Procedures Used to Estimate Key Model Parameters

Parameter	Independent Calculation	Selection Procedure
Bed void fraction at coal inlet, ϵ_c, and ash outlet, ϵ_a	Void fractions can be measured or estimated from coal and ash properties. Typical values may range between 0.2 and 0.8 depending on particle distribution, sphericity and particle roughness.*	Bed void fraction is selected to match measured pressure profile. Initially, ϵ_c and ϵ_a are adjusted in equal increments; however, top or bottom void fractions are adjusted independently if the measured profile indicates a larger or smaller void fraction.
Solid-to-gas heat-transfer correction factor, ζ	Selection of ζ is based on experience with the sensitivity analysis shown in Figures 4 and 5. A value of 0.1 is recommended if no other data are available.	ζ is selected to match the location of the maximum measured temperature.
Effective diffusivity parameter, $\phi = \phi_a/\tau^2 \approx \phi_a/2$	ϕ can be measured or estimated from the ash porosity, ϕ_a. Ash porosities range from 0.06 to 0.60 for ash obtained from fixed-bed gasifiers (see Hobbs, 1990). An acceptable range for ϕ might be 0.02 to 0.5. A value of 0.5 is recommended if no other data are available.	ϕ can be selected to match the location of the maximum measured temperature. ϕ is usually adjusted after ζ is chosen. If adjusting ζ is insufficient to adjust the location of the maximum temperature, adjust ϕ.
SP or AS model option	Selection of the char model is based on experience with the sensitivity analysis as shown in Figure 3C. The SP model option is recommended if no other data are available.	The AS model can be chosen, if a discontinuity is observed in the measured pressure profile, if the oxidation zone is very small with a corresponding steep temperature gradient, or if burnout is high simultaneously with a large drying zone as is common for lignites with high moisture contents.

*Fayed and Otten (1984) discuss bed void fraction. For spherical particles, bed void fraction for close random packing ranges from 0.359 to 0.375; for hexagonal close packing, bed void fraction is 0.26. The effect of nonsphericity is to increase bed void fraction. For example, for a sphere with a sphericity of 1.0, it is 0.4; for a cube with sphericity 0.8, it is 0.5; and for a particle with sphericity of 0.2 it is 0.85.

Comparisons with Fixed-Bed Data

Selection of model variables

While effluent gas composition is predicted by MBED-1D, comparison of these predicted and measured values does not provide a strong evaluation of a generalized fixed-bed model. Once coal burnout is established, which is often near unity, and tar production is estimated (for example, Ko et al., 1988), effluent gas composition can be readily estimated without recourse to a generalized, fixed-bed model (Hobbs et al., 1992). Thus, evaluation of MBED-1 was performed by comparison with measured axial profiles of temperature and pressure in fixed beds. No data for composition profiles were located for this purpose, and experimental temperature and pressure profiles within laboratory or commercial-scale fixed-bed gasifiers are limited. Eight low-pressure, air-blown Wellman-Galusha cases (Thimsen et al., 1984) were simulated together with one high-pressure, oxygen-blown Lurgi gasifier case with Rosebud subbituminous coal. No measured profiles were available for the dry-ash Lurgi gasifier.

These simulations are also compared to predictions from other one-dimensional models. Measured and predicted solid temperatures for several operating conditions are also compared for some of the Wellman-Galusha tests. Comparisons of predicted and experimental temperature profiles have helped to determine recommended values of model parameters. Caution must be exercised, however, when making conclusions based on profiles from experimental fixed-bed data. Thimsen (1990) warns that temperature profiles for the Wellman-Galusha cases be used for qualitative comparisons only, since the temperature probe [1/2-in. (13-mm) schedule 40 304 SS pipe with six sheathed type-K thermocouples placed 6 in. (152 mm) apart] was retracted from the gasifier when any junction approached 1,600 K. Typically, the temperature probe was allowed 10 minutes to reach steady state (Thimsen et al., 1984). Furthermore, the temperature profiles may represent transient conditions if the probes were retracted early. The usual disadvantages related to intrusive probes may also cause problems in fixed-bed temperature measurements: physical processes may be altered by flow disturbances; catalytic perturbations may be caused by the probe; and radiation and/or conduction losses may be significant. The measured temperature profiles were assumed to be closer to the solid temperature following Barriga and Essenhigh (1980). Additional simulations predicted concentration profiles of major and minor species, carbon consumption rates due to oxidation and gasification, burnout, and particle diameter.

A solid-to-gas heat-transfer correction factor of 0.1 was used for all simulations. The effective diffusivity was assumed to equal 0.5 times the molecular diffusivity. The bed void distribution was assumed to vary linearly between the top and bottom of the bed, as supported by the data from Krishnudu et al. (1989). Bed void fractions were not measured directly for any of the cases. Void fractions of the feed coal at the bed top and the product ash at the bed bottom were estimated based on coal and ash bulk and apparent density measurements.

Wellman-Galusha dry-ash gasifier

Predicted axial variations in temperature and pressure profiles are compared to measurements for gasification of the eight coals in the Wellman-Galusha gasifier in Figures 8 and 9. Profile comparisons for both temperature and pressure are considered to be quite good for all, but the lignite case. Measurements for the Jetson case indicate the location of the maximum temperature. Predicted axial variations in temperature, pressure drop, gas concentration, oxidation/gasification carbon consumption rate, burnout, and particle diameter for atmospheric gasification of the Jetson bituminous coal are shown in Figure 10. This case is presented in detail since it was used as the base case in the sensitivity analysis. In the Jetson case, burnout (daf) was predicted to be unity as shown in Figure 10F. Thus, carbon is not available for oxidation in the ash zone. The ash zone temperature remains approximately 550 K. Carbon becomes available for oxidation approximately 0.5 m from the bottom of the reactor where oxidation begins. The highly exothermic oxidation reaction increases the solid temperature dramatically. The oxidation reaction occurs before the steam gasification reaction, as shown by the carbon consumption rates in Figure 10E. Once initiated, the endothermic steam gasification reaction causes the positive solid temperature gradient to decrease. This competition between exothermic and endothermic reactions describes the initial step in the temperature profile going from the ash zone to the oxidation zone.

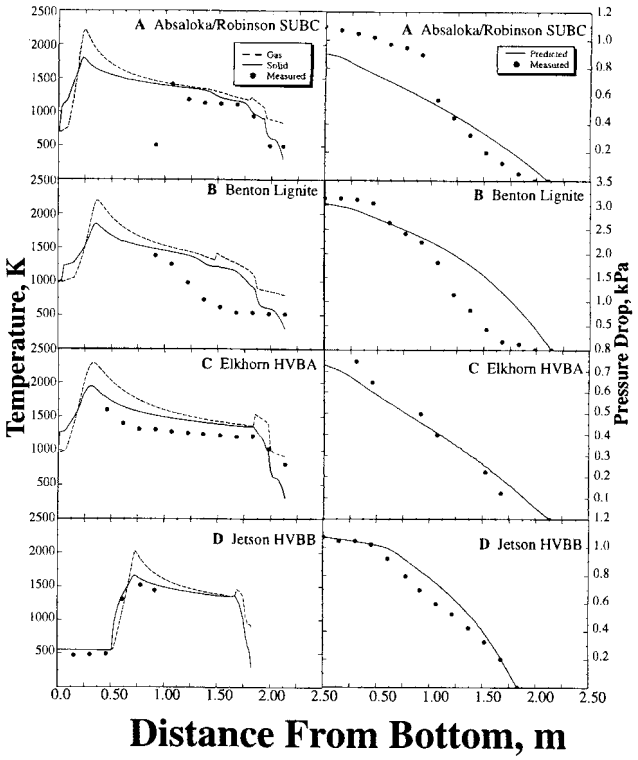

Figure 8. Predicted and measured axial variations in temperature and pressure drop during gasification of: A) Absaloka/Robinson subbituminous; B) Benton lignite; C) Elkhorn bituminous; and D) Jetson bituminous coals in an air-blown, atmospheric Wellman-Galusha gasifier.

Measurements are from Thimson et al. (1984). Input parameters are in Tables 3, 4, 7 and 8.

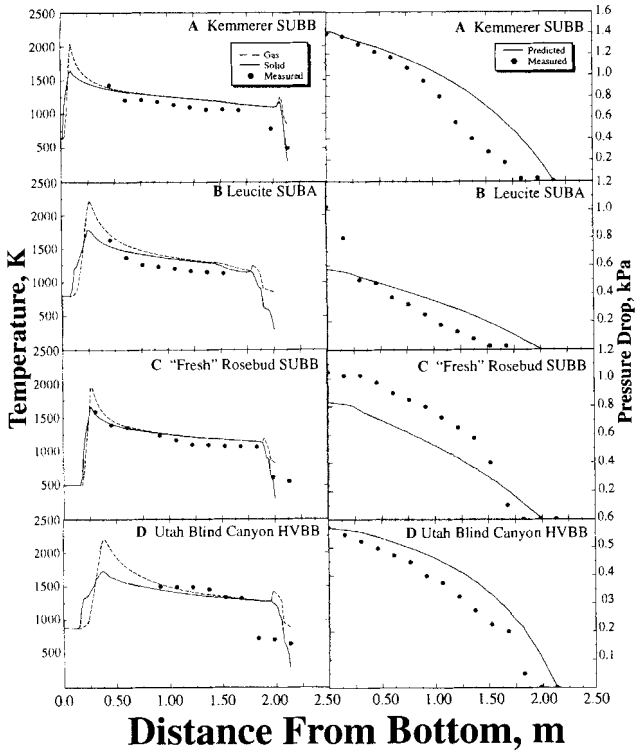

Figure 9. Predicted and measured axial variations in temperature and pressure drop during gasification of: A) Kemmerer subbituminous; B) Leucite subbituminous; C) "fresh" Rosebud subbituminous; and D) Utah Blind Canyon bituminous coals in an air-blown, atmospheric Wellman-Galusha gasifier.

Measurements are from Thimsen et al. (1984). Input parameters are in Tables 3, 4, 7 and 8.

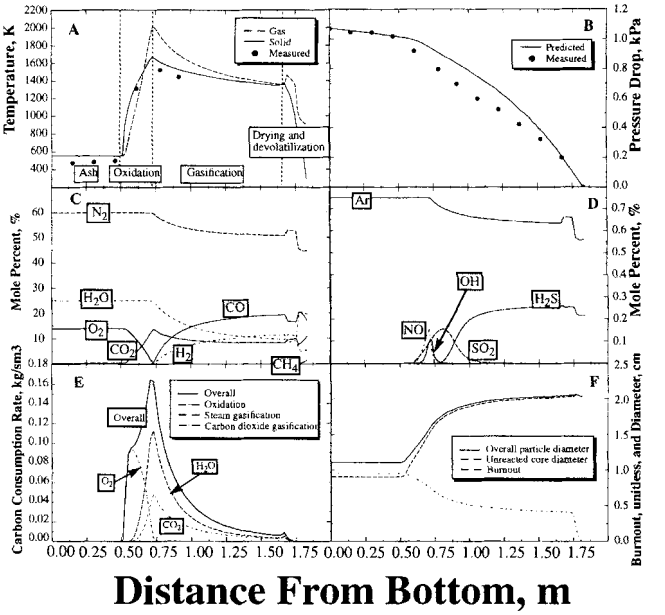

Figure 10. Predicted axial: A) temperature; B) pressure drop; C) major species concentration; D) minor species concentration; E) oxidation/gasification carbon consumption rate; and F) burnout, overall and unreacted particle diameter in an atmospheric air-blown Wellman-Galusha gasifier with Jetson bituminous coal.

Input parameters are in Tables 3, 4, 7 and 8. Measurements are from Thimsen et al. (1984, Vol. 2, p. K5).

The temperature is highest at the end of the oxidation zone and starts to decrease due to predominantly endothermic gasification reactions of carbon with steam and carbon dioxide in the gasification zone.

Steam gasification overlaps oxidation as shown in Figure 10E. For example, at 0.65 m from the reactor bottom, the carbon consumption rate due to steam gasification is approximately 0.05 kg/s·m^3. At this location in the reactor, steam is reacting with carbon to produce hydrogen and carbon monoxide. However, no depletion of steam is observed in the concentration profile at this reactor location as shown in Figure 10C. Steam is being replenished by the homogeneous oxidation of hydrogen. Also, carbon monoxide produced from both oxidation and steam gasification is being oxidized in the presence of oxygen to produce carbon dioxide. Carbon dioxide reaches a maximum at the end of the oxidation zone and decreases in the gasification zone. In the gasification zone, carbon dioxide reacts heterogeneously with carbon to produce carbon monoxide. Carbon monoxide is not present in the gas phase until oxygen is depleted. As with carbon monoxide, hydrogen does not appear in the gas phase until oxygen is depleted. Although agreement between the predicted and measured pressure profiles was acceptable, the void distribution may not be linear throughout the reactor. For example, the measured pressure profile in Figure 10B indicated that the void fraction changed markedly near the ash zone.

The predicted increase in the particle diameter at the top of the reactor was due to coal particle swelling. Swelling was assumed to be proportional to the extent of devolatilization. For the Jetson case, the predicted particle diameter of the ash was about 1.1 cm. The measured geometric mean diameter of the ash was 1.02 cm as reported by Thimsen et al. (1984). The excess nitrogen and high temperatures caused the equilibrium quantities of NO and OH to form in the oxygen-rich, high-temperature zone of the reactor. These quantities decayed to zero as temperature decreased. Sulfur dioxide also formed in the presence of oxygen and was converted to H_2S in the colder, fuel-rich regions of the gasifier.

Several of the Wellman-Galusha experimental test cases included temperature profiles at different operating conditions. Predicted temperature profiles were compared to measurements for the Elkhorn, the Jetson, the Leucite Hills and the Utah Blind Canyon coals in Figure 11. A shift in the measured temperature profile due to changing reactant feed rates during gasification of Elkhorn bituminous coal is shown in Figure 11A. The predicted trends agreed with the direction of the measured temperature shifts in each case. From the sensitivity analysis, an increase in coal flow rate caused the location of the maximum temperature to move closer to the bottom of the reactor. In general, an increase in either the steam flow rate or air flow rate caused the location of the maximum temperature to move closer to the top of the reactor. In this

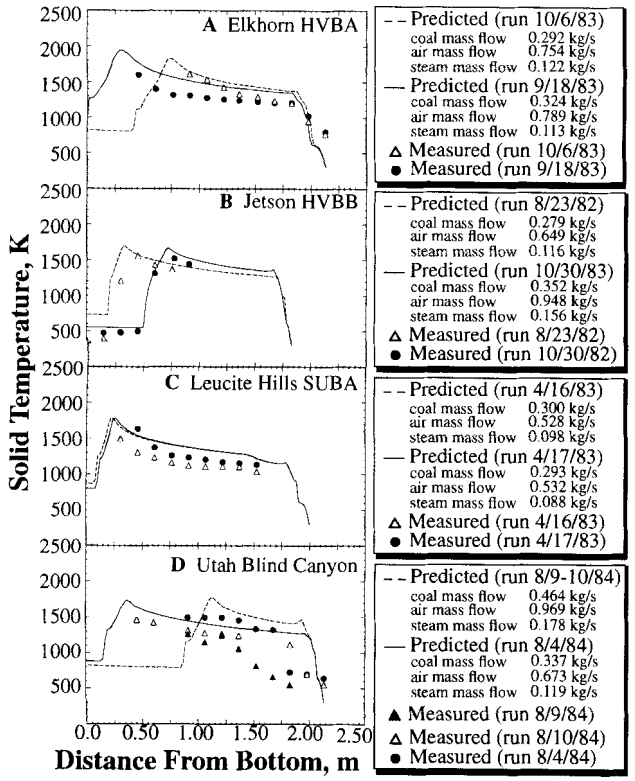

Figure 11. Measured temperature vs. predicted solid temperature for several operating conditions for gasification of: A) Elkhorn bituminous; B) Jetson bituminous; C) Leucite Hills subbituminous; and D) Utah Blind Canyon bituminous coals in an air-blown, low-pressure Wellman-Galusha gasifier.

Experimental data are in Thimsen et al. (1984). Input parameters are listed in the legend and in Tables 3, 4, 7 and 8.

case, the coal and the air flow rates were both increased, the steam flow rate was decreased, and the location of the maximum temperature moved toward the reactor bottom. Although the increased air flow rate should have caused the location of the maximum temperature to move toward the reactor top, changes in coal and steam flow rates were more significant for the Elkhorn case.

The effect of varying feed rates on the location of the maximum temperature is shown in Figure 11B for gasification of Jetson bituminous coal. The direction of the temperature shift was predicted adequately by the one-dimensional model. An increase in the coal, air and steam mass-flow rates caused the location of the maximum temperature to move toward the top of the reactor. For the Jetson case, the increase in steam and air mass-flow rates was more significant than the increase in the coal mass flow rate. Although the low-rank coals were more difficult to simulate, predictions from the one-dimensional model agreed with the experimental data for the Leucite Hills subbituminous coal as shown in Figure 11C. The increase in coal flow rate and decrease in steam flow rate caused the location of the maximum temperature to shift toward the bottom of the reactor for the Leucite Hills case. The Utah Blind Canyon case in Figure 11D also showed the effect of increased coal and gas throughputs. Trends in measured and predicted profiles do not agree for this case. However, the measurements were repeated on two separate days, but only one set of operational data was reported for this time period (Thimsen et al., 1984), possibly explaining variability in the data.

Lurgi dry-ash gasifier

Predicted axial temperature, pressure drop, gas concentration, carbon consumption rates due to oxidation and gasification, burnout, and particle diameter are shown in Figure 7 for the Lurgi gasifier fired with Rosebud subbituminous coal. The most obvious difference compared to results from the atmospheric air-blown gasifier was the absence of a carbon dioxide peak. The shape of the carbon dioxide profile was due to the low temperature of the solid in the gasification section, resulting from large quantities of steam in the feed gas stream. The temperature was low enough that the only significant heterogeneous reaction in this section of the gasifier was the steam gasification reaction. With only hydrogen and carbon monoxide being produced in the gasification section, the hydrogen and carbon monoxide profiles should have been similar. However, gas-phase reactions such as the water-gas-shift reaction produced a slight increase in carbon dioxide concentration.

Temperature predictions from two other one-dimensional models are also shown in Figure 7A. These cases were reported to be the Illinois #6 Westfield case (Yoon, 1978; Cho, 1980). However, the input conditions differed from those reported by Elgin and Perks (1974) and seemed to be closer to the Rosebud case. The source of Yoon's input data is uncertain. Also, Cho (1980) used the values provided by Yoon (1978). Yoon assumed equal solid and gas temperature, instantaneous devolatilization with a fixed composition, and gas-phase chemistry dominated by the water-gas-shift reaction. Cho essentially extended the model of Yoon to include separate solid and gas temperatures. The Yoon prediction was similar to the prediction made in our work. The shape of the solid temperature profile predicted by Cho is similar to the solid profile predicted here. Cho's gas temperature profile, however, does not correspond to the predictions by Yoon or this study. Cho's gas temperatures were less than the solid temperature in the oxidation zone. The gas temperature will be less when important gas-phase reactions are neglected. For example, steam gasification will produce H_2 and CO in the oxidation zone, and CO will be produced from oxidation. In the presence of oxygen, the homogeneous reactions of H_2 and CO with O_2 will react to produce H_2O, CO_2, and heat. These exothermic gas-phase reactions will cause a dramatic increase in gas temperature as shown in the predictions of this study.

Insights Into Fixed-Bed Gasification

Resistances to char oxidation and gasification

Chemical reaction resistance ($\propto 1/k_r\zeta$), ash diffusion resistance ($\propto 1/k_{\text{eff}}$), and film diffusion resistance ($\propto 1/k_m$) illustrate the dominant chemical and physical processes occurring in fixed-bed reactors. Resistances for char oxidation and gasification of the base case are shown in Figure 12. Chemical resistances dominate at the top and bottom of the reactor for the oxidation and gasification reactions. The ash resistance was highest at the reactor bottom. At the top of the reactor,

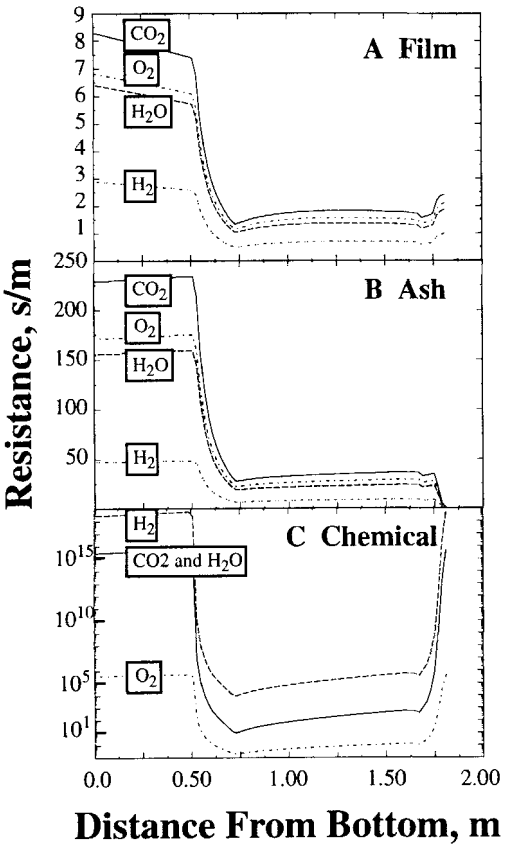

Figure 12. Resistances for char oxidation and gasification of Jetson coal in an atmospheric fixed-bed gasifier: A) film resistance; B) ash resistance; and C) chemical resistance to char oxidation and gasification reactions.

These plots correspond to the Jetson case in Figure 10.

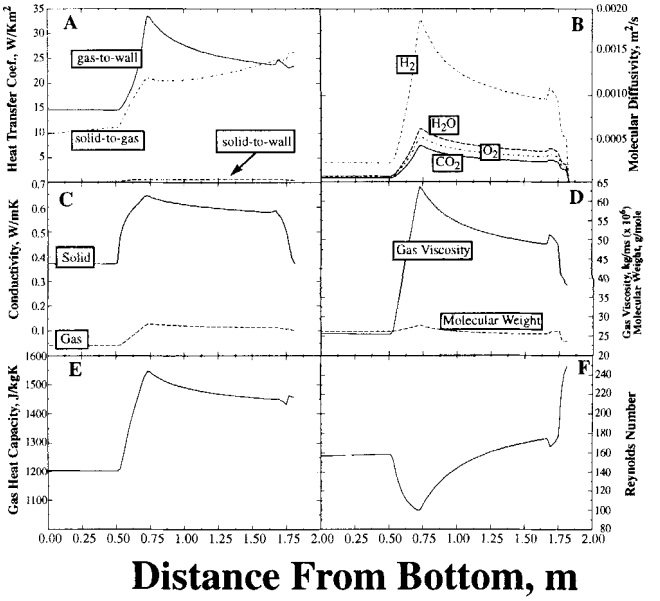

Figure 13. Predicted heat-transfer coefficients and transport properties for gasification of Jetson coal in an atmospheric Wellman-Galusha gasifier with air: A) heat-transfer coefficients; B) molecular diffusivities; C) solid and gas conductivities; D) gas viscosity and molecular weight; E) gas heat capacity; and F) Reynolds numbers.

These plots correspond to the Jetson case in Figure 10.

no ash layer was present. Once the ash layer was sufficiently thick, ash diffusion competed with the chemical reaction resistance in the gasification section of the gasifier as shown in Figures 12B and 12C. Although confidence in calculated mass-transfer coefficients was generally greater than confidence in chemical reaction coefficients, ash porosity was not measured throughout the reactor, and the effective ash diffusivity was difficult to predict.

Transport properties

Predicted heat-transfer and -transport coefficients for the base case are shown in Figure 13. Typical values for the overall bed-to-wall heat-transfer coefficient range from 15-35 $W/m^2 \cdot K$. The bed-to-wall heat-transfer coefficient can be divided into contributions from the gas-to-wall coefficient and solid-to-wall coefficient, as shown in Figure 13A. Over 95% of the heat loss to the wall for this case was due to the gas phase. The large heat transfer from the gas phase was caused by a high effective radial gas conductivity. The gas conductivity was dominated by a large dynamic contribution due to the high gas velocities. Gas Reynolds numbers throughout the reactor are shown in Figure 13F. The solid and gas conductivities are shown in Figure 13C. The solid conductivity was assumed to be proportional to the square root of solid temperature (Table 2, Eq. 7). The gas mixture conductivity was calculated from classical methods. Changes in gas conductivity, gas heat capacity, and gas viscosity were somewhat similar through the bed, all rising sharply with rapid increase in gas temperature, as shown in Figures 13C-13E.

Solid and gas residence time, velocity and heating rate

Solid residence time for the base case was on the order of hours as shown in Figure 14A. The corresponding gas residence time was on the order of seconds. The solid residence time increases in the ash zone due to significant settling resulting in variable axial velocity. Axial solid and gas velocities were shown in Figure 14B. Gas velocities were less than 3 m/s. Solid velocities were less than 0.1 mm/s. Solid velocity was affected by mass loss due to drying and devolatilization. The solid velocity decreases as heterogeneous oxidation and gasification reactions consumed the solid mass. With mass loss, the particle diameter decreased and the corresponding particle number density increased. Once all reactions were quenched, the solid velocity remained constant. Although mass addition to the gas phase contributed to increased gas velocity, temperature effects probably were more significant.

Gas and solid heating rates depend on the axial temperature profile and solid and gas residence times. Gas heating rates are approximately 4 orders of magnitude higher than the solid heating rate due to different residence times. Significant changes in heating rate occur at the oxidation temperature spike and

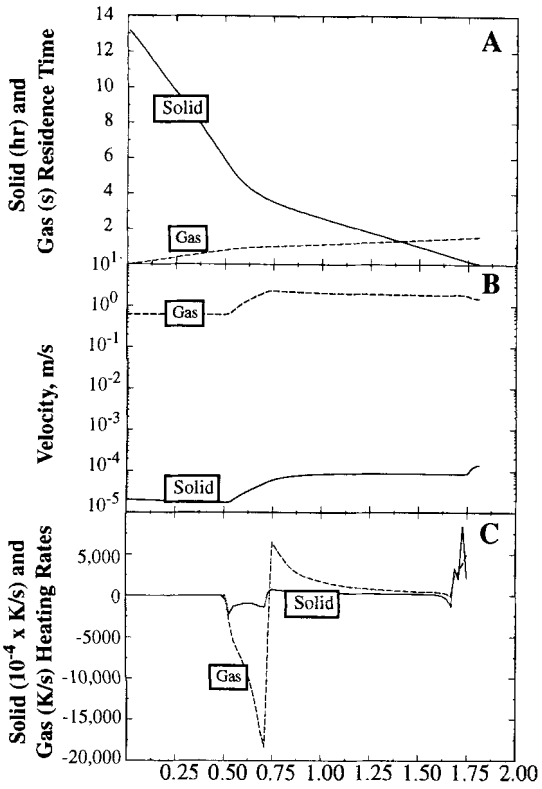

Figure 14. Predicted solid and gas: A) residence times; B) velocities; and C) heating rates during gasification of Jetson bituminous coal in an air-blown, atmospheric Wellman-Galusha gasifier.

These plots correspond to the Jetson case in Figure 10.

in the devolatilization zone where rapid heterogeneous reactions occur.

Summary and Conclusions

A generalized, one-dimensional fixed-bed gasification/combustion model (MBED-1D) has been formulated, solved numerically, evaluated through parametric sensitivity analysis, and compared with measured fixed-bed axial temperature and pressure profiles. Model advances and/or characteristics include separate gas and particle temperatures, simultaneous drying, coal devolatilization, char oxidation and gasification zones, generalized gas-phase chemistry, axially variable bed void fraction and gas/solid flow rates, and generalized, coal-independent rate-controlled devolatilization. Solution times on a midlevel computer workstation are only a few minutes.

Predictions from the MBED-1D are compared to temperature and pressure measurements from a commercial-scale Wellman-Galusha dry-ash gasifier. Predicted axial temperature and pressure profiles, using a common set of model parameters, compared well with the measured values for many coals. A suitable estimate of bed void distribution was shown to be necessary to predict the pressure drop throughout the reactor. A linear increase in bed void fraction from the top to the bottom of the reactor was found to be sufficient for most calculations. The void distribution dramatically influences volumetric reaction rates through the particle number density.

From temperature profile comparisons, higher coal feed rates or processes, which cause the gas phase to become fuel-richer, also cause the location of the maximum temperature to move toward the bottom of the reactor. Such processes include: cracking of tar in the gasification and devolatilization zones; increasing devolatilization rate by neglecting volatiles transport; and increasing the volatile content through changes in coal type, moisture content, or ash content. Devolatilization is not instantaneous, and volatile yield significantly affects the temperature profile and the location of the maximum temperature. Various dips and peaks in the axial temperature profile correspond to different functional groups that evolve at different temperatures. Furthermore, a dual temperature peak may result during high-pressure gasification as a result of competing endothermic and exothermic reactions. Oxidation and gasification do not occur in separate zones, but simultaneously in the reactor bed. Furthermore, results suggest that solid-to-gas heat transfer for reacting fixed beds is significantly smaller than for nonreacting fixed beds. Diffusional resistance of oxidizer through the ash layer during oxidation and gasification was predicted to be significant.

Important model parameters whose values are not well established were identified. These include the solid-to-gas heat-transfer coefficient, ash layer thickness and oxidizer diffusivity through the char-ash layer, and the variable bed void fraction. The effective diffusivity of oxidizer through the ash layer is a complex function of the developing ash porosity and tortuosity which is not likely to be constant throughout the reactor. Future research should include the effect of coal structure, mineral matter, devolatilization and bed burden on the effective diffusivity.

Acknowledgment

This work was sponsored principally by the U. S. Department of Energy, Morgantown Energy Technology Center (Contract No. DE-AC21-86MC23075) under subcontract from Advanced Fuel Research, Inc., East Hartford, and in part by the Advanced Combustion Engineering Research Center at Brigham Young University. Funds for this center are received from the National Science Foundation's Engineering Centers, the State of Utah, 25 industrial participants, and the U. S. Department of Energy. Help from Dr. M. Usman Ghani is also acknowledged. Helpful suggestions and comments by the reviewers are also acknowledged.

Notation

A = cross-sectional area of reactor, m^2
A = particle surface area, m^2
A = preexponential factor, m/s·K
A = water wall surface area, m^2
C = carbon
C = molar concentration of oxidizer or gasification agent, $kmol/m^3$
C_p = specific heat, J/kg·K
d = particle diameter, m
D = diffusivity, m^2/s
D = reactor diameter, m
E = activation energy, J/kmol
F = fraction of original carbon (Eq. 9), mass fraction
g = acceleration of gravity, 9.80665 m/s^2
G = superficial gas mass flux, $kg/m^2 \cdot s$
h = enthalpy, J/kg
h = heat-transfer coefficient, $W/m^2 \cdot K$

H = convective heat capacity flux, J/m^2·s
H = hydrogen
k = rate and Arrhenius rate constant, m/s or 1/s
k = thermal conductivity, W/m·K
k = mass transport coefficient, m/s
L = reactor length, m
$\dot{m}$ = mass flow rate, kg/s
Mw = molecular weight, kg/kmol
N = nitrogen
O = oxygen
P = pressure, kPa, Pa
Pe = Peclet number (Table 2)
Pr = Prandtl number (Table 2)
Q = heat loss, W/m^3
r = volumetric reaction rate, kg/m^3·s
R = ideal gas constant, J/kmol·K
Re = Reynold's number (Table 2)
S = sulfur
Sc = Schmidt number (Table 2)
t = time, s
T = temperature, K
u = velocity, m/s
V = volatile matter, mass fraction
V = volume, m^3
VM = volatile matter, mass fraction
W = mass-flow rate, kg/s
x = gas mole fraction
x = tar fraction, mass fraction
x = tar parameter used in correlation of Ko et al. (1988)
y = functional group fraction, mass fraction
z = axial distance, m

Greek letters

ϵ = bed void fraction, void vol./bed vol.
ϵ' = emissivity
ϕ = packing parameter defined by Eq. 10 in Table 2
ϕ = porosity, vol./vol.
η = particle number density, 1/m^3
κ = ratio of solid conductivity and gas conductivity
λ = stoichiometric coefficient for oxidation reaction, mol/mol
μ = viscosity, kg/m·s
ν = stoichiometric coefficient, mol carbon/mol oxidant
ρ = density, kg/m^3
Ω = dry, ash-free mass fraction
ω = functional group fraction or element fraction, mass fraction
ζ = bed-to-wall heat-transfer multiplier (for sensitivity analysis)
ζ = particle area factor to account for internal surface burning
ζ = reacting to nonreacting solid-to-gas heat-transfer ratio
τ = tortuosity

Subscripts

a = ash
BG = blast gas
c = char
c = coal
CO_2 = CO_2 gasification
e = effective
e = equilibrium
eff = effective
g = gas
gw = gas-to-wall
H_2 = H_2 gasification
H_2O = H_2O gasification
hw = heat transfer to the wall
i = index for elements, species, or reactions
j = index for solid species
m = mass transport
m = mixture
m = molecular
nonvol C = nonvolatile carbon
nonvol S = nonvolatile sulfur
o = initial
O_2 = oxidation
p = particle
r = radial
r = radiative
r = reaction
s = solid
s = steam
sg = solid-to-gas
sm = solid measured (refers to the apparent density)
sw = solid-to-wall
t = tar
t = total
u = unreacted core
v = void
v = volatiles
w = wall
w = water
x = tar
z = axial

Superscripts

a = axial thermal
d = devolatilization
g = gas
h = thermal
m = axial mass
o = initial
o = reference temperature
o = static
s = sensible enthalpy
s = solid
t = true
ultimate = yield at large times
∞ = infinity or ultimate

Literature Cited

Amundson, N. R., and L. E. Arri, "Char Gasification in a Countercurrent Reactor," *AIChE J.*, **24**, 87 (1978).

Barriga, A., and R. H. Essenhigh, "A Mathematical Model of a Combustion Pot: Comparison of Theory and Experiment," Paper 80-WA/HT-32, ASME Meeting, Chicago (1980).

Baxter, L. L., personal communication, Brigham Young Univ., Provo (1987).

Bhattacharya, A., L. Salam, M. P. Dudukovic, and B. Joseph, "Experimental and Modeling Studies in Fixed-Bed Char Gasification," *Ind. Eng. Chem. Process Des. Dev.*, **25**, 988 (1986).

Bird, R. B., W. E. Stewart, and E. N. Lightfoot, *Transport Phenomena*, Wiley, New York (1960).

Bischoff, K. B., "A Note on Gas Dispersion in Packed Beds," *Chem. Eng. Sci.*, **24**, 607 (1962).

Blackwood, J. D., "The Reaction of Carbon with Hydrogen at High Pressure," *Aust. J. Chem.*, **12**, 14 (1959).

Cho, Y. S., *Modeling and Simulation of Lurgi-type Gasifiers*, MS Thesis, Washington Univ., St. Louis, MO (1980).

Cho, Y. S., and B. Joseph, "Heterogeneous Model for Moving-Bed Coal Gasification Reactors," *Ind. Eng. Chem. Process Des. Dev*, **20**, 314 (1981).

Crowe, C. T., and L. D. Smoot, "Multicomponents Conservation Equations," *Pulverized-Coal Combustion and Gasification*, L. D. Smoot and D. T. Pratt, eds., Plenum Press, New York (1979).

Desai, P. R., and C. Y. Wen, "Computer Modeling of the MERC Fixed Bed Gasifier," MERC/CR-78/3, U. S. Dept. of Energy, Morgantown, WV (1978).

DeWasch, A. P., and G. F. Froment, "A Two-Dimensional Heterogeneous Model for Fixed Bed Catalytic Reactors," *Chem. Eng. Sci.*, **26**, 629 (1971).

Dzhapbyev, K., A. L. Miropol'skii, and V. J. Mal'kovskii, "Investigation of Unsteady Heat Transfer in a Packed Bed of Spheres Swept by Gas," *Thermal Eng.*, **33**(3), 159 (1986); translated from *Teploenergetika*, **33**(3), 70 (1986).

Earl, W. B., and K. A. Islam, "Steady-state Model of a Lurgi-type Coal Gasifier," *Innovation in the Process and Resource Industry, CHEMCA*, Proc. Australian Chem. Eng. Conf., Perth, Australia, Paper c2b, 289 (1985).

Elgin, D. C., and H. R. Perks, "Results of Trials of American Coals in Lurgi Pressure-Gasification Plant at Westfield, Scotland," *Synthetic Pipeline Gas Symp.*, Chicago (Oct. 18-20, 1974).

Ergun, S., "Fluid Flow Through Packed Columns," *Chem. Eng. Prog.*, **48**, 89 (1952).

Fayed, M. E., and L. Otten, eds., *Handbook of Powder Science and Technology*, Van Nostrand Reinhold, New York (1984).

Field, M. A., D. W. Gill, B. B. Morgan, and P. G. W. Hawksley, *Combustion of Pulverized Coal*, The British Coal Utilization Res. Assoc., Leatherhead, England (1967).

Fletcher, T. F., A. R. Kerstein, R. J. Pugmire, M. S. Solem, and D. M. Grant, "A Chemical Percolation Model for Devolatilization: 3. Chemical Structure as a Function of Coal Type," *Energy and Fuels*, submitted (1992).

Froberg, R. W., "*The Carbon-Oxygen Reaction: an Experimental Study of the Oxidation of Suspended Carbon Spheres*," PhD Diss., Pennsylvania State Univ., University Park (1967).

Froment, G. F., and K. B. Bischoff, *Chemical Reactor Analysis and Design*, Wiley, New York (1979).

Goetz, G. J., N. Y. Nsakala, R. L. Patel, and T. C. Lao, "Combustion and Gasification Characteristics of Chars from Four Commercially Significant Coals of Different Rank," final report 165-6, EPRI, Palo Alto, CA (1982).

Gray, D. D., and J. M. Stiles, "On the Constitutive Relation for Frictional Flow of Granular Materials," topical report DOE/MC/21353-2584, U. S. Dept. of Energy, Morgantown, WV (1988).

Gray, D., J. G. Cogoli, and R. H. Essenhigh, "Problems in Pulverized Coal and Char Combustion," *Adv. Chem. Ser.*, **131**, 72, (1974).

Gupta, A. S., and G. Thodos, "Direct Analogy Between Mass and Heat Transfer to Beds of Spheres," *AIChE J.*, **9**(6), 751 (1963).

Hedman, P. O., L. D. Smoot, P. J. Smith, and A. U. Blackham, "Entrained-Flow Gasification at Elevated Pressure," DOE/MC/22059-2570, Combustion Laboratory, Chemical Engineering Dept., Brigham Young Univ., Provo (1987).

Hindmarsh, A. C., "ODEPACK, A Systematized Collection of ODE Solvers," *Scientific Computing*, R. S. Stepleman, ed., Vol. 1, p. 55, IMACS Trans. on Scientific Computation, North-Holland, Amsterdam (1983).

Hobbs, M. L., "*Modeling Countercurrent Fixed-Bed Coal Gasification*," PhD Diss., Brigham Young Univ., Provo (1990).

Hobbs, M. L., P. T. Radulovic, and L. D. Smoot, "Prediction of Effluent Temperatures and Compositions for Fixed-Bed Coal Gasifiers," *Fuel*, accepted (1992).

Khanna, R., and J. H. Seinfeld, "Mathematical Modeling of Packed Bed Reactors: Numerical Solutions and Control Model Development," *Advances in Chemical Engineering*, J. Wei, J. L. Anderson, K. B. Bischoff, M. M. Denn, and J. H. Seinfeld, eds., Vol. 13, p. 113, Academic Press (1987).

Kim, M., and B. Joseph, "Dynamic Behavior of Moving-Bed Coal Gasifiers," *Ind. Eng. Chem. Process Des. Dev.*, **22**, 212 (1983).

Ko, G. H., D. M. Sanchez, W. A. Peters, and J. B. Howard, "Correlations for Effects of Coal Type and Pressure on Tar Yields from Rapid Devolatilization," *Symp. Int. on Combustion*, p. 115, The Combustion Institute, Pittsburgh (1988).

Krishnudu, T., B. Madhusudhan, S. N. Reddy, V. S. R. Sastry, K. S. Rao, and R. Vaidyeswaren, "Studies in a Moving Bed Pressure Gasifier: Prediction of Reaction Zones and Temperature Profile," *Ind. Eng. Chem. Res.*, **28**, 438 (1989).

Kunii, D., and J. M. Smith, "Heat Transfer Characteristic of Porous Rocks," *AIChE J.*, **6**(1), 71 (1960).

Kurylko, L., "*The Unsteady and Steady Combustion of Carbon*," PhD Diss., The Pennsylvania State Univ., University Park (1969).

Laurendeau, N. M., "Heterogeneous Kinetics of Coal Char Gasification and Combustion," *Prog. Energy Combust. Sci.*, **4**, 221 (1978).

Lowry, H. H., *Chemistry of Coal Utilization*, Supple. Vol. Wiley, New York (1963).

Merrick, D., "Mathematical Models of the Thermal Decomposition of Coal: 2. Specific Heats and Heats of Reaction," *Fuel*, **62**, 540 (1983).

Mills, K. C., and J. M. Rhine, "The Measurement and Estimation of the Physical Properties of Slags Formed During Coal Gasification: 2. Properties Relevant to Heat Transfer," *Fuel*, **68**, 201 (1989).

Nsakala, N., R. L. Patel, and T. C. Lao, "Combustion Characterization of Coals for Industrial Applications," Final Technical Report for U. S. Dept. of Energy, Pittsburgh, Combustion Engineering Inc., Kreisinger Development Laboratory, Winsor, CT, DOE/PC/402067-5 (DE85010673) (Mar. 1985).

Nuttall, H. E., W. G. Stoddart, and W. J. Chen, "Pyrolysis of Subbituminous New Mexico Coal," *J. of Petr. Tech.*, **31**, 418 (1979).

Park, K. Y., and T. F. Edgar, "Modeling of Early Cavity Growth for Underground Coal Gasification," *Ind. Eng. Chem. Res.*, **26**, 237 (1987).

Perry, R. H., and C. H. Chilton, eds., *Chemical Engineers' Handbook*, 5th ed., McGraw-Hill, New York (1973).

Phuoc, T. X., and M. P. Mathur, "Transient Heating of Coal Particles Undergoing Pyrolysis," *Combust. and Flame*, **85**, 380 (1991).

Radulovic, P. T., M. L. Hobbs, and L. D. Smoot, "Fixed-Bed Coal Combustion and Gasification Review," *Prog. Energy Combust. Sci.*, submitted (1992).

Rohsenow, W. M., J. P. Hartnett, and E. N. Ganic, *Handbook of Heat Transfer Applications*, McGraw-Hill, New York (1985).

Saxena, S. C., "Devolatilization and Combustion Characteristics of Coal Particles," *Prog. Energy Combust. Sci.*, **16**, 55 (1990).

Serio, M. A., D. G. Hamblen, J. R. Markham, and P. R. Solomon, "Kinetics of Volatile Product Evolution in Coal Pyrolysis: Experiment and Theory," *Energy & Fuels*, **1**, 138 (1987).

Smith, I. W., "The Combustion Rates of Coal Chars: a Review," *Int. Symp. on Combustion*, p. 1045, The Combustion Institute, Pittsburgh (1983).

Smoot, L. D., and P. J. Smith, *Coal Combustion and Gasification*, Plenum Press, New York (1985).

Smoot, L. D., and P. J. Smith, *Pulverized-Coal Combustion and Gasification*, p. 224, L. D. Smoot and D. T. Pratt, eds., Plenum, Press, New York (1979).

Solomon, P. R., D. G. Hamblen, R. M. Carangelo, M. A. Serio, and G. Y. Deshpande, "General Model of Coal Devolatilization," *Energy and Fuels*, **2**, 405 (1988).

Stillman, R., "Simulation of a Moving Bed Gasifier for a Western Coal," *IBM J. Res. Dev.*, **23**, 240 (1979).

Stull, D. R., and H. Prophet, *JANAF Thermochemical Tables*, 2nd ed., National Bureau of Standards (1971).

Suuberg, E. M., W. A. Peters, and J. B. Howard, "Product Compositions and Formation Kinetics in Rapid Pyrolysis of Pulverized Coal—Implications for Combustion," *Int. Symp. on Combustion*, p. 177, The Combustion Institute, Pittsburgh (1979).

Thimsen, D., personal communications (1990).

Thimsen, D., R. E. Maurer, A. R. Pooler, D. Y. H. Pui, B. Y. H. Liu, and D. B. Kittelson, "Fixed-Bed Gasification Research using U. S. Coals," **1-19**, U. S. Bureau of Mines Contract H0222001, final report (1984).

Thorsness, C. B., and S. W. Kang, "Further Development of a General-Purpose, Packed-Bed Model for Analysis of Underground Coal Gasification Processes," *Underground Coal Gasification Symp.*, Denver (1985).

Thorsness, C. B., and S. W. Kang, "A General-Purpose, Packed-Bed Model for Analysis of Underground Coal Gasification Processes," UCID-20731, Lawrence Livermore National Laboratory, Univ. of California, Berkeley (1986).

Thorsness, C. B., S. W. Kang, "A Method-of-line Approach to Solution of Packed-bed Flow Problems Related to Underground Coal Gasification Processes," *Underground Coal Gasification Symp.*, Williamsburg, VA (1984).

Walker, P. L., F. Rusinko, and L. G. Austin, *Advances in Catalysis*, p. 134, D. D. Eley, P. W. Selwood, and P. B. Weisz, eds., **XI**, Academic Press, New York (1959).

Wang, S. C., and C. Y. Wen, "Experimental Evaluation of Non-isothermal Solid-Gas Reaction Model," *AIChE J.*, **18**(6), 1231 (1972).

Wen, C. Y., and T. Z. Chaung, "Entrainment Coal Gasification Modeling," *Ind. Eng. Chem. Process Des. Dev.*, **18**(4), 684 (1979).

Wen, C. Y., H. Chen, and M. Onozaki, *User's Manual for Computer Simulation and Design of the Moving Bed Coal Gasifier*, final report

prepared for Morgantown Energy Technology Center, U. S. Dept. of Energy, DOE/MC/16474-1390, Morgantown, WV (1982).
Winslow, A. M., "Numerical Model of Coal Gasification in a Packed Bed," *Int. Symp. on Combustion*, p. 503, The Combustion Institute, Pittsburgh, (1976).
Yagi, S., and D. Kunii, "Studies on Heat Transfer Near Wall Surface in Packed Beds," *AIChE J.*, **6**(1), 97 (1960).
Yagi, S., D. Kunii, and N. Wakao, "Studies on Axial Effective Thermal Conductivities in Packed Beds, *AIChE J.*, **6**(4), 543 (1960).
Yagi, S., and N. Wakao, "Heat and Mass Transfer from Wall to Fluid in Packed Beds," *AIChE J.*, **5**(1), 79 (1959).
Yoon, H., "Modeling and Analysis of Moving Bed Coal Gasifiers," PhD Diss., Univ. of Delaware, Newark (1978).
Yoon, H., J. Wei, and M. M. Denn, "A Model for Moving-bed Coal Gasification Reactors," *AIChE, J.*, **24**(5), 885 (1978).
Yu, W., M. M. Denn, and J. Wei, "Radial Effects in Moving Bed Coal Gasifiers," *Chem. Eng. Sci.*, **38**, 1467 (1983).

Manuscript received Aug. 9, 1991, and revision received Mar. 5, 1992.